Research Paper

# Optimal parameter design of a slot jet impingement/microchannel heat sink base on multi-objective optimization algorithm

H.C. Cui, C.Y. Shi, M.J. Yu, Z.K. Zhang, Z.C. Liu, W. Liu[*]

*School of Energy and Power Engineering, Huazhong University of Science and Technology, Wuhan 430074, China*

A B S T R A C T

Jet impingement and microchannel cooling as effective cooling methods have been widely employed for thermal management of high heat flux electronics. In this work, a novel hybrid slot jet impingement/microchannel heat sink, combining the advantages of two cooling technologies, was proposed to achieve vertical flushing of the jet and timely discharge of the waste fluid. To further enhance the cooling performance, a 3-D numerical simulation was applied to evaluate the impact of inlet and outlet branch passage inclination ratios ($H_{in,1}/H_{in,2}$ and $H_{out,1}/H_{out,2}$), channel unit width ($W_1$), channel width ratio ($\varphi$) and channel height ($H_3$) on heat sink thermal-hydraulic characteristics. According to the parametric analysis, the variations in the inlet and outlet branch passage inclination ratios have significant effect on the mass flow distribution among the heat transfer channels. Afterward, to acquire the optimal compromise solution for practical applications, the artificial neural network training and multi-objective optimization algorithms, i.e. multi-objective particle swarm optimization (MOPSO) and multi-objective genetic algorithm (MOGA), are utilized to optimize the geometrical parameters, i.e. $W_1$, $\varphi$ and $H_3$. During the optimization, the average heated surface temperature ($\overline{T}_{heat}$) and the total pressure drop ($\Delta P$) are two conflicting objectives to evaluate the heat transfer and resistance characteristics. Finally, an optimal compromise solution ($W_1$ = 1.03 mm, $\varphi$ = 0.58 and $H_3$ = 2.44 mm) is chosen from the Pareto front by using the classical decision-making algorithm, i.e. TOPSIS. Compared with one objective minimization in the Pareto front, the optimal compromise solution has a sound balance between heat transfer and resistance performance. Additionally, for the optimal compromise solution, with an inlet velocity of 1.5 m/s and a heat flux of 200 W/cm$^2$, the maximum and average temperature of the heated surface does not exceed 73 °C and 67 °C, respectively, and the total pressure drop is only 5.7 kPa.

## 1. Introduction

Along with the continuous development of IT, electronic products are ubiquitous in modern society. These electronic products provide convenience and comfort for people's life while also leading to huge energy consumption. Take the rapid development of artificial intelligence technology for example, the processing of huge amounts of data has increasingly higher requirements on the computing power of chips. Nevertheless, the increased computing power and functionality of the chip results in greater heat generation [1,2]. As the microfabrication techniques evolve, the shift to miniaturization and integration have further exacerbated the heat dissipation problems, which has become the major roadblock to future IC development. Faced with this situation, more energy, i.e. higher velocity or lower temperature of the coolant, needs to be used to maintain the safe working temperature of

electronics, which exacerbates the energy consumption problem. According to published data, the heat flux in some traditional integrated circuits has reached 100 W/cm$^2$ [3], while in some special electronics, i. e. advanced radar [4], high-power IGBT (Insulated Gate Bipolar Transistor) and high-power laser diode arrays [5], the heat flow can reach 500 W/cm$^2$. Moreover, as transistor densities continue to rise, the heat flux is expected to reach even higher levels in the foreseeable future for some electronics. Consequently, it is imperative to study and propose advanced and efficient cooling technologies. In contrast with traditional cooling technologies, jet impingement cooling and microchannel cooling are considered as the prospective methods to address the heat dissipation issues of high heat flux in the future due to their remarkable cooling capacity [6].

In 1981, Tuckerman and Pease first proposed the conception of microchannel heat sink and pointed out that applying this cooling technique can substantially enhance cooling performance by reducing

**Nomenclature**

| | |
|---|---|
| $C_{1\varepsilon}, C_{2\varepsilon}$ | constants for turbulence model |
| $c_p$ | specific heat at constant pressure (J·kg$^{-1}$·K$^{-1}$) |
| $D$ | diameter (m) |
| $e$ | the relative error |
| $f$ | the fitting function |
| $h$ | heat transfer coefficient (W·cm$^{-2}$·K$^{-1}$) |
| $H$ | height (m) |
| $J$ | objective function |
| $k$ | thermal conductivity (W·m$^{-1}$·K$^{-1}$) or turbulence kinetic energy (J) |
| $L$ | length (m) |
| $\dot{m}$ | coolant mass flow rate (g·s$^{-1}$) |
| $N$ | the number of grids |
| $P$ | total pressure (Pa) |
| $p$ | the apparent order |
| $q$ | heat flux of the heated surface (W·cm$^{-2}$) |
| $R^2$ | regression coefficient |
| $Re$ | Reynolds number |
| $r$ | the refinement ratio |
| $S$ | the heat transfer area (mm$^2$) or the mean rate-of-strain tensor (s$^{-1}$) |
| $T$ | temperature (K, °C) |
| $u, v, w$ | velocity (m·s$^{-1}$) |
| $W$ | width (m) |
| $w$ | the weighting factor |
| $x, y, z$ | orthogonal coordinate system |

*Greek symbols*

| | |
|---|---|
| $\rho$ | density (kg·m$^{-3}$) |
| $\varepsilon$ | dissipation rate of turbulence kinetic energy |
| $\sigma_k, \sigma_\varepsilon$ | turbulent Prandtl numbers for $k$ and $\varepsilon$ |
| $\lambda_{eff}$ | effective thermal conductivity (W·m$^{-1}$·K$^{-1}$) |
| $\mu$ | dynamic viscosity (Pa·s) |
| $\eta, \eta_t$ | dynamic viscosity and eddy viscosity (Pa·s) |
| $\nu$ | kinematic viscosity (m$^2$·s$^{-1}$) |
| $\phi, \varphi$ | the numerical results (K, Pa) and channel width ratio |

*Subscript*

| | |
|---|---|
| $ave$ | the average value |
| $f$ | average value of inlet and outlet |
| $heat$ | the heated surface |
| $inlet, in$ | the heat sink inlet or inlet branch passage |
| $outlet, out$ | the heat sink outlet or the outlet branch passage |
| $s$ | solid domain |
| $t$ | total heat transfer area |
| $w$ | the heat transfer surface |

*Abbreviations*

| | |
|---|---|
| ANN | artificial neural network |
| GCI | grid convergence index |
| MSE | mean square error |
| MOGA | multi-objective genetic algorithm |
| MOPSO | multi-objective particle swarm optimization |
| SJIMHS | slot jet impingement/microchannel heat sink |

heat transfer resistance [7]. By etching microchannels at the silicon substrate, a heat flux of 790 W/cm$^2$ could be successfully dispelled while the maximum substrate temperature rise is no higher than 71 °C above the inlet water temperature. In the following decades, the microchannel cooling technology, with its excellent cooling capacity, has inspired scholars all over the world to carry out a large number of numerical and experimental investigations to further evaluate the impacts of structural parameters, e.g. channel shape [8–11], hydraulic diameter [12], flow pattern [13] and spoiler structure [14–17], on heat transfer characteristics. Although microchannel cooling technology has a large specific surface area, compact structure and smaller footprint, the large temperature and pressure gradients in the flow path become the major limitations to its applications, particularly prominent at long channel lengths [18]. The main reasons for the temperature gradient are that the cooling medium temperature gradually increases in the flow direction and the heat transfer coefficient decreases with a thicker boundary layer [19], while the main causes of the pressure gradient are the small hydraulic diameter and long channel lengths.

Jet impingement cooling technology is also considered as one of the most prospective liquid cooling technologies because of its outstanding cooling capacity, i.e. good synergy between velocity and temperature fields, intense fluid disturbance and high heat transfer coefficient. Kiper [20] was one of the pioneers in considering jet impingement cooling as a promising method for cooling electronics. In experiments with VLSI (very large scale integration) circuit using submerged liquid jet array cooling, the heat transfer coefficient of jet array cooling was observed to be remarkably higher than traditional liquid cooling techniques such as microchannel cooling and immersion cooling. In recent years, to further explain the essence of jet impingement heat transfer and to improve the cooling performance, a large number of numerical and experimental studies have been conducted to investigate the impacts of jet hole shape [21], jet hole arrangement and diameter [22], jet-to-target spacing [23,24] and enhanced surface type [25] on thermal-hydraulic

characteristics. Although lower pressure drop and higher heat transfer coefficient could be realized with jet impingement cooling technology, the heat transfer coefficient is more unevenly distributed [18]. Additionally, the lack of heat transfer area does not allow the advantages of high-speed jet to be fully utilized [26].

Based on the above literature studies, both cooling methods have their own advantages and disadvantages, and seem to complement each other. For instance, the microchannel cooling technology has a large specific area, but a high pressure loss. The jet impingement cooling technology has a relatively low pressure loss, but a small heat transfer area. Consequently, it has been proposed that two cooling methods can be integrated to design a novel cooling heat sink that takes full advantage of both. In 2006, Mudawar and Sung [27] found that the combination of microchannel and jet impingement cooling can achieve a much higher heat dissipation capacity. Inspired by the research of Sung, Zhang et al. [28] numerically examined the impact of microchannel shape, i.e. rectangular, trapezoid and circular, on the cooling capability of hybrid jet impingement and microchannel heat sink. To better evaluate the cooling capability and flow resistance characteristics of the hybrid mini channel and slot jet array scheme, Deng et al. [29] examined the hybrid scheme experimentally and numerically, and compared its cooling performance with independent slot jet array heat sink and mini channel heat sink. To solve the adverse effect of horizontal cross flow, Zhou et al. designed a novel slot jet impingement/microchannel heat sink successfully used it for SiC/GaN wide bandgap inverter heat dissipation in electric vehicles [30,31]. By applying the manifold system, the microchannels were separated into segments to shorten the coolant flow path and discharge the waste coolant. Different from the manifold system adopted by Zhou, Robinson et al. used micro-3D metallic printing technology to prepare a hybrid microjet-microchannel heat sink [32]. By confining the impinging microjets within the individual cells, the problems of wall jet formation and horizontal cross flow deteriorating heat transfer performance are solved. To further improve the cooling

capability of the hybrid heat sink, the introduction of enhanced structures into microchannels has been proposed by some scholars [33–35]. The enhanced structures not only increase the total heat transfer area, but may also improve the cooling capability through boundary layer interruption, flow mixing and turbulent transport [36,37].

According to above literature research, the hybrid cooling scheme incorporates the merits of the two cooling technologies and exhibits superior heat transfer performance. However, there are still some issues needed to be solved. First, when the channel length is long or the heat transfer surface is large, the impacts of horizontal cross flow prevent the jet near the outlet from vertically washing against the heat transfer surface [38], resulting in uneven temperature distribution along the channel. Although some novel designs have been proposed in recent years to ensure that the spent fluid can be extracted timely, most of them are more complex and have higher processing costs [32,39]. Besides, geometry parameters of the microchannel and jet show significant impact on the thermal-hydraulic characteristics of hybrid heat sinks, but fewer studies have used specialized mathematical optimization algorithms to search for the optimum of key structural parameters. In practical applications, more attention is paid to the optimal structural design for specific scenarios. Additionally, since most structural parameter variations lead to contradictory changes in heat transfer and flow resistance performance, it is impossible to select the optimal combination of structure parameters from a wide range of parameters without professional meritocratic algorithms. Considering the increasing energy consumption for electronics heat dissipation in future [40], any slight improvement of the heat sink cooling performance will produce significant financial benefits.

Therefore, based on the previous literature research, this work designs a novel hybrid slot jet impingement/microchannel heat sink to achieve vertical flushing of the jet and timely discharge of the spent fluid. Additionally, the influences of structural parameters, i.e. inlet/outlet branch passage inclination, channel height, channel unit width and channel width ratio, on cooling capability and flow resistance

characteristics have been investigated numerically. Subsequently, a combination of artificial neural network training and genetic algorithm is adopted for multi-objective optimization of the key geometric parameters. Different from traditional parametric analysis, the multi-objective optimization used in this work can optimize the contradictory objectives simultaneously and the optimization result obtained from algorithm is a set of non-inferior solutions. Finally, an optimal compromise solution is chosen from the Pareto front by using the classical decision-making algorithm, which achieves the optimal balance of heat transfer and resistance performance.

## 2. Numerical methodology

### 2.1. Geometric model and variable settings

Fig. 1 presents the 3-D model of the hybrid slot jet impingement/microchannel heat sink (SJIMHS) simulated in this work, which includes the top cover plate and the heat transfer plate. The detailed dimensions that correspond to each part are given in Table 1, and the determination of the cooling area refers to Ref. [41]. The inlet and outlet branch passages are machined on the top cover plate to distribute the cooling medium and evacuate the spent fluid timely, respectively. Rectangular microchannels are manufactured on the heat transfer plate, which

**Table 1**
Geometrical parameters of SJIMHS (Units: mm, except for $\varphi$).

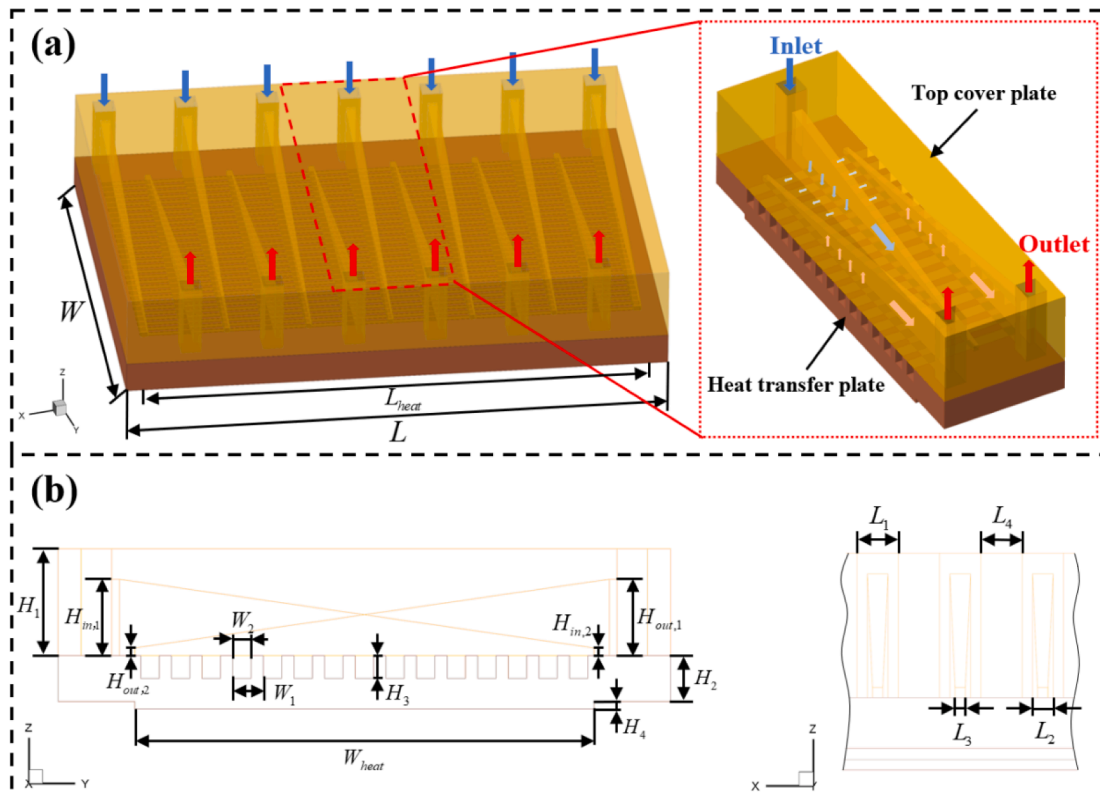| $L$ | $W$ | $L_{heat}$ | $W_{heat}$ | $L_1$ | $L_2$ | $L_3$ | $L_4$ |
|---|---|---|---|---|---|---|---|
| 53 | 40 | 49 | 30 | 2 | 1 | 0.5 | 2 |
| $W_1$ | | $\varphi = \dfrac{W_2}{W_1}$ | | $H_1$ | $H_2$ | $H_3$ | $H_4$ |
| 1/1.5/2/2.5/3 | | 0.4/0.5/0.6/0.7/0.8 | | 7 | 3 | 0.5/1/1.5/2/2.5 | 0.5 |
| $H_{in,1}$ | | $H_{in,2}$ | | $H_{out,1}$ | | $H_{out,2}$ | |
| 3/4/5/6 | | 0.5/3/6 | | 3/4/5/6 | | 0.5/3/6 | |



**Fig. 1.** (a) Hybrid slot jet impingement/microchannel heat sink 3-D model; (b) Detailed dimensions of each part.

integrates with the top cover plate to form the fluid path. The flow path inside the heat sink is illustrated in Fig. 1(a). Typically, the cooling medium enters in from the heat sink inlet and passes through inlet branch passages to achieve a uniform fluid distribution, after that the fluid washes against the wall of the microchannel and exits through the outlet branch passages. The alternating arrangement of the inlet and outlet branch passages enables short-distance transport and timely discharge of fluid in the rectangular microchannel, avoiding horizontal cross flow induced by the accumulation of spent fluid in the flow direction. In addition, copper with excellent thermal conductivity is used as the base material for each part, and water is used as the cooling medium.

### 2.2. Governing equations and simulation setups

Based on literature research, the Realizable $k - \varepsilon$ model has relatively high accuracy in the prediction of cooling capability and flow resistance characteristics of jet impingement/microchannel heat sinks [28]. Additionally, several turbulence models are used to calculate the slot jet impingement/microchannel heat sink model of the previous literature, and the simulation results are compared with the experimental results in the literature, as presented in Section 2.6. The comparison results point out that the Realizable $k - \varepsilon$ model has the best prediction accuracy and moderate computational cost. As a result, the Realizable $k - \varepsilon$ model with enhanced wall treatment is selected for subsequent calculations. Additionally, it is supposed that the flow is steady-state, continuous and incompressible to simplify the calculation. The flow resistance and cooling performance of the hybrid scheme are calculated using the commercial software Fluent 16.0, and the governing equations in the fluid domain are given below:

Continuity equation:

$$\frac{\partial(\rho u_i)}{\partial x_i} = 0 \tag{1}$$

Momentum conservation equation:

$$\frac{\partial(\rho u_i u_j)}{\partial x_j} = -\frac{\partial p}{\partial x_i} + \frac{\partial}{\partial x_j}\left(\mu \frac{\partial u_i}{\partial x_j} - \rho \overline{u_i' u_j'}\right) \tag{2}$$

Energy conservation equation:

$$\frac{\partial(u_i T)}{\partial x_j} = \frac{\partial}{\partial x_j}\left(\frac{\lambda_{eff}}{\rho c_p}\frac{\partial T}{\partial x_j}\right) \tag{3}$$

Kinetic energy equation:

$$\frac{\partial}{\partial x_i}(\rho k u_i) = \frac{\partial}{\partial x_j}\left[\left(\eta + \frac{\eta_t}{\sigma_k}\right)\frac{\partial k}{\partial x_j}\right] + 2\eta_t \frac{\partial u_i}{\partial x_j}S_{i,j} - \rho\varepsilon \tag{4}$$

Dissipation rate equation:

$$\frac{\partial}{\partial x_i}(\rho k u_i) = \frac{\partial}{\partial x_i}\left[\left(\eta + \frac{\eta_t}{\sigma_\varepsilon}\right)\frac{\partial \varepsilon}{\partial x_i}\right] + C_{1\varepsilon}\rho S\varepsilon - C_{2\varepsilon}\rho \frac{\varepsilon^2}{k + \sqrt{\nu\varepsilon}} \tag{5}$$

where $p$ is the pressure, $\rho$ is the liquid density, $u_i$ is the speeds in the $x$, $y$, $z$ direction, $\eta$ is the dynamic viscosity, $\nu$ is the kinematic viscosity, $\eta_t$ is the eddy viscosity, $S$ is the modulus of the mean rate-of-strain tensor, $c_p$ is the constant pressure specific heat capacity, $\sigma_k$ and $\sigma_\varepsilon$ are the turbulent Prandtl numbers for $k$ and $\varepsilon$. $S_{i,j}$ and $C_{1\varepsilon}$ are given by the following equation, where $C_{2\varepsilon}$, $\sigma_k$ and $\sigma_\varepsilon$ are 1.92, 1 and 1.2 respectively.

$$S_{i,j} = \frac{1}{2}\left(\frac{\partial u_i}{\partial x_j} + \frac{\partial u_j}{\partial x_i}\right) \tag{6}$$

$$S = \sqrt{(2S_{i,j}S_{i,j})} \tag{7}$$

$$C_{1\varepsilon} = \max\left\{0.43, \frac{\overline{\mu}}{5 + \overline{\mu}}\right\} \tag{8}$$

The governing equation in the solid domain:

$$\frac{\partial}{\partial x_i}\left(k_s \frac{\partial T}{\partial x_i}\right) = 0 \tag{9}$$

where $k_s$ is the thermal conductivity of the copper.

Since the entire model is symmetric about the $x$-axis, half of the whole heat sink is chosen as the computational model with the symmetric boundary condition, as depicted in Fig. 2. In addition, the heat sink inlet is set as the velocity inlet with a constant velocity of 6 m/s and a constant temperature of 20 °C, and the corresponding inlet Reynolds number is about 11880. The pressure outlet is used for the heat sink outlet. Constant heat flux is set to the heated surface, which has an area of $49 \times 30$ mm$^2$. The no slip boundary condition is employed to the solid-liquid interface, and the adiabatic boundaries are adopted to the rest of walls. The determination of the boundary conditions refers to our previous experimental and numerical studies [26,42].

The classical pressure-velocity coupling algorithm, i.e. SIMPLE, is used to discrete the governing equation. As for the spatial discretization, the standard discretization is adopted for pressure, QUICK for energy, and second-order upwind for the rest. Additionally, the convergence criterion for the continuum equation and momentum equation is $10^{-5}$, $10^{-7}$ for the energy equation and $10^{-4}$ for the turbulence equation.

### 2.3. Physical properties parameters

As mentioned above, the hybrid heat sink simulated in this work is made of cooper with excellent thermal conductivity, i.e. $k_s = 387.6$ W/(m·K). Pure water is adopted as the cooling medium and the variation of its properties with temperature is represented by following equations.

Density (kg/m$^3$): $\rho = -0.003369T^2 + 1.733T + 779.7$;

Thermal conductivity (W/(m·K)): $\lambda = -1.298 \times 10^{-5}T^2 + 0.009629T - 1.108$;

Specific heat (J/(kg·K)): $c_p = 0.01131T^2 - 7.095T + 5290$;

Viscosity (kg/(m·s)): $\mu = 1.462 \times 10^{-7}T^2 - 0.0001049T + 0.01917$.

### 2.4. Data reduction

In the numerical simulation, choosing suitable performance indicators to assess the effects of different structural parameter variations is necessary. To reduce the impact of heat transfer area changes on subsequent performance comparisons, the average heat transfer coefficient, i.e. $\overline{h}$, is defined on the basis of the heated surface area instead of the heat transfer area. The expression is defined as follows:

$$\overline{h} = \frac{q}{\overline{T}_{trans} - T_f} \tag{10}$$

where $q$ is the constant heat flux of the heated surface, $\overline{T}_{trans}$ is the average temperature of the heat transfer surface and $T_f$ is the average temperature of the heat sink inlet and outlet.

The inlet Reynolds number is expressed as:

$$Re_{inlet} = \frac{\rho u_{in} D_{in}}{\mu} \tag{11}$$

where $D_{in}$ is the hydraulic diameter of the heat sink inlet, which can be expressed as $D_{in} = \frac{2L_1 L_1}{L_1 + L_1}$.

The pressure drop inside the heat sink is defined as:

$$\Delta P = P_{inlet} - P_{outlet} \tag{12}$$

$$\Delta P_1 = P_{inlet} - P_{jetin} \tag{13}$$

$$\Delta P_2 = P_{jetin} - P_{jetout} \tag{14}$$

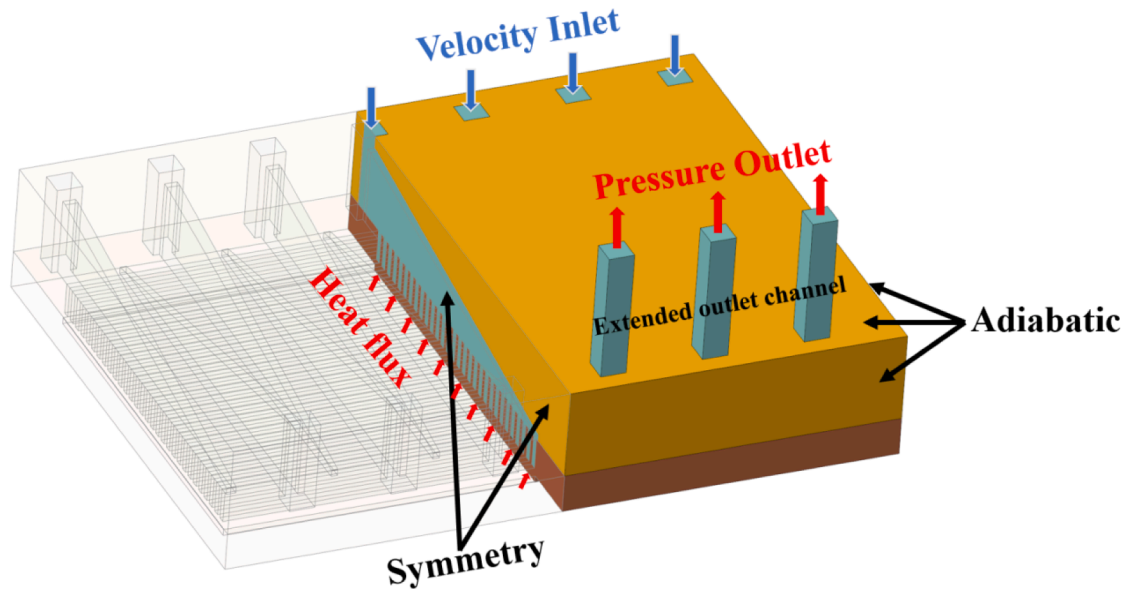$$\Delta P_3 = P_{jetout} - P_{outlet} \tag{15}$$

**Fig. 2.** Three-dimensional computation model.

where $P_{inlet}$ is the average total pressure of the heat sink inlet, $P_{outlet}$ is the average total pressure of the heat sink outlet, $P_{jetin}$ is the average total pressure of the slot jet inlet and $P_{jetout}$ is the average total pressure of the slot jet outlet. Consequently, the $\Delta P, \Delta P_1$, $\Delta P_2$ and $\Delta P_3$ is employed to evaluate the heat sink total pressure drop and resistance losses in inlet/outlet branch passages and heat transfer microchannels, respectively.

### 2.5. Meshing strategy and grid independence verification

Fig. 3 shows the assembly diagram of the overall mesh and the local mesh refinement information of the liquid region. Given the effects of back flow on simulation results, the outlet channel is lengthened to $5D_{outlet}$ ($D_{inlet/outlet} = L_1$). The commercial software ICEM 16.0 is used to generate hexahedral mesh for each part, and the interface coupled is used for the mesh intersection of each part. To fulfill the demands of the near-wall function, i.e. $y^+ \approx 1$, and improve the calculation accuracy as much as possible, the liquid-solid contact surface is refined and the first mesh layer height is set as 0.01 mm and the mesh growth factor is set as

1.2. The zoom-in views of mesh in the inlet and outlet slot jet region and the near wall region can be visualized by slicing the mesh longitudinally. Fig. 3(b) portrays the grid refinement of the liquid region including the outlet extension.

During the grid independence verification, the number of grids is varied by adapting the maximum cell size while keeping the near-wall region refinement conditions constant. To avoid the influence of the number of grid on calculation results as much as possible, three sets of grids were calculated with the number of $N_1 = 19, 179, 532, N_2 = 11, 268, 576$, and $N_3 = 4, 364, 959$, respectively. The heat sink structure parameters used for grid independence verification are $W_1 = 2$ mm, $\varphi = 0.6$, $H_3 = 1.5$ mm, $H_{in,1} = H_{out,1} = 5$ mm and $H_{in,2} = H_{out,2} = 0.5$ mm, respectively. Fig. 4(a) depicts the temperature variation along the $x$-axis for three sets of grids corresponding to the heat transfer surface. Obviously, the trend of temperature variation is the same when the number of girds changes, and the biggest difference in temperature between different grids does not exceed 1 K. Additionally, the total pressure drop and average temperature of the heat transfer surface are depicted in Fig. 4(b). Visibly, by increasing the grid numbers from $N_2$ to
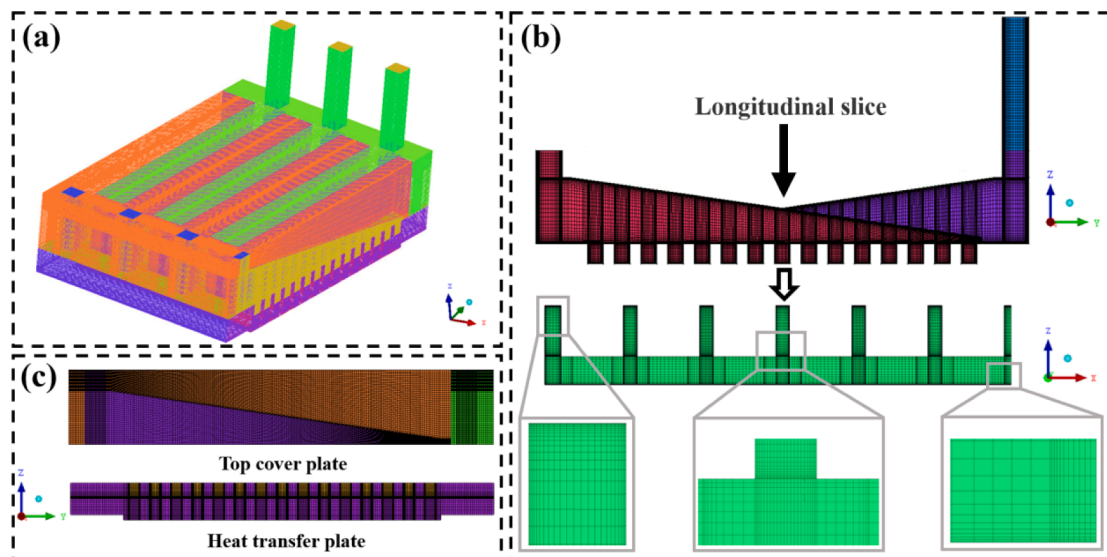


**Fig. 3.** The overall mesh of SJIMHS in (a) and the refined mesh of each part in (b) and (c).
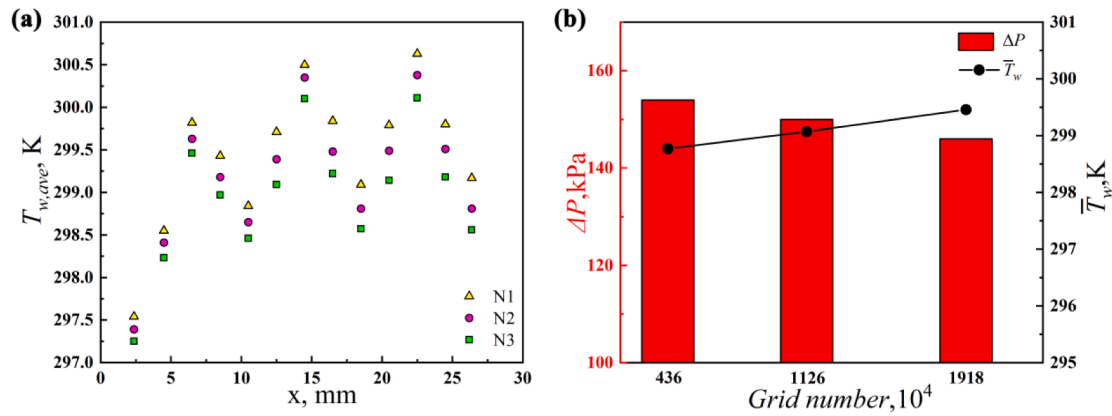
**Fig. 4.** (a) Comparison of the temperature distribution along the *x*-axis of the heat transfer surface; (b) Comparison of the total pressure drop and average temperature of the heat transfer surface.

$N_1$, the relative errors of pressure drop and temperature are less than 3.2% and 0.15%, respectively, which has met the accuracy requirement. Furthermore, the grid independence was verified by utilizing the Grid Convergence Index (GCI) method, which gives an error band estimate of the discretization errors on solution quantities [43]. As shown in Table 2, the refinement ratio between grids $N_1$ and $N_2$ as well as between grids $N_2$ and $N_3$ are defined by $r_{21}$ and $r_{32}$, respectively. The solution results of the average temperature of the heat transfer surface and total pressure drop are demonstrated by $\phi_1$, $\phi_2$ and $\phi_3$ for each respective grid. In addition, the detail information about the observed order ($p$), extrapolated value ($\phi_{ext}^{21}$) and relative error ($\phi_a^{21}$ and $\phi_{ext}^{21}$) can be found in literature [43]. Based on the calculation formula, the GCI for the grid $N_2$ ($GCI_{fine}^{21}$) were calculated and the results show that there is an $0.1 \sim 3\%$ error band on the average temperature and pressure drop due to discretization. Therefore, the same meshing strategies as the grid $N_2$ are adopted for the subsequent calculations when the structural parameter changes.

## 2.6. Turbulence model verification

In numerical simulation, a suitable viscous model is essential for the accuracy of the numerical simulation. According to literature research, the Reynolds-average Navier-Stokes (RANS) and Large Eddy Simulation (LES) methods have been used to simulate the cooling capability and flow resistance characteristics inside the microchannel or jet impingement heat sink [18,44]. It has been proved that the LES model has the better accuracy in capturing the flow characteristics near the wall [45] and investigating the unsteady behavior of the fluid. Nevertheless, compared with the RANS turbulence model, LES requires more computational resources and has a relatively longer computational cycle. Considering that this work pays more attention to the heat

**Table 2**
Grid Convergence Index (GCI) verification.

|  | $\phi = \overline{T}_w [K]$ | $\phi = \Delta P [Pa]$ |
|---|---|---|
| $N_1, N_2, N_3$ | 19,179,532, 11,268,576, 4,364,959 | 19,179,532, 11,268,576, 4,364,959 |
| $r_{21}$ | 1.213 | 1.213 |
| $r_{32}$ | 1.35 | 1.35 |
| $\phi_1$ | 299.46 | 145,617 |
| $\phi_2$ | 299.07 | 150,345 |
| $\phi_3$ | 298.77 | 154,566 |
| $p$ | 5.46 | 4.22 |
| $\phi_{ext}^{21}$ | 299.67 | 141,869 |
| $e_a^{21}$ | 0.13% | 3.25% |
| $e_{ext}^{21}$ | 0.07% | 2.64% |
| $GCI_{fine}^{21}$ | 0.09% | 3.22% |

transfer characteristics of heat sinks in steady state, the RANS turbulence models with moderate computational cost are more suitable in this work.

Sung et al. [46] experimentally investigated the single-phase and two-phase cooling capability of hybrid microchannel/slot-jet impingement heat sink. In their hybrid configuration, the size of slot jet and microchannel are $2.94 \times 0.6 \times 1.65$ mm and $20 \times 1 \times 3$ mm respectively, which are comparable to the heat sink dimensions examined in this work. Considering the computational efficiency, one unit of the hybrid heat sink is adopted in the single-phase simulation and the computational model and boundary conditions are presented in Fig. 5 (a). In addition, the boundary conditions are in accordance with the Ref. [46]. Three turbulence models, i.e. RNG $k - \varepsilon$, Realizable $k - \varepsilon$ and SST$k - \omega$, are adopted and the numerical results of temperatures along thermocouple line are compared with measured values, shown in Fig. 5 (b). The thermocouple line is 5.08 mm above the heated surface and the *x*-axis origin is in the middle of the slot jet. As demonstrated in Fig. 5(b) and Table 3, the temperature increases gradually in the flow direction and the Realizable $k - \varepsilon$ model has the best matching performance with experimental results. Additionally, the Ref. [28,47–49] also shows that the Realizable $k - \varepsilon$ model is suited to calculate the cooling performance and resistance characteristics of the hybrid jet impingement/microchannel heat sink. Consequently, the Realizable $k - \varepsilon$ model is subsequently adopted for further numerical simulations in this study.

## 2.7. Geometric parameter optimization method

### 2.7.1. Multi-objective optimization algorithm and optimization process

According to the parametric analysis, it is found that the change of geometric parameters will significantly affect the cooling capability and flow resistance characteristics, and there may be a coupling effect between the parameters. Consequently, it is not reasonable to acquire the optimal parameter merely through parametric analysis, and specialized mathematical optimization algorithms are required to obtain the optimal parameter combination. As an effective method to optimize multiple conflicting objectives, Multi-objective optimization algorithm optimizes the objective functions simultaneously instead of combining objective functions into a compound function. In addition, the optimization result obtained from optimization algorithm is not a specific solution, but a set of non-inferior solutions.

Multi-objective particle swarm optimization (MOPSO) and multi-objective genetic algorithm (MOGA) are two commonly used multi-objective optimization algorithms, which are employed in this study to provide credible Pareto solutions. MOGA is a multi-objective evolution algorithm based on the genetic iteration [50], implying that solutions will compete with each other and generate the next generation based on fitness values. With the evolutionary procedure going, the
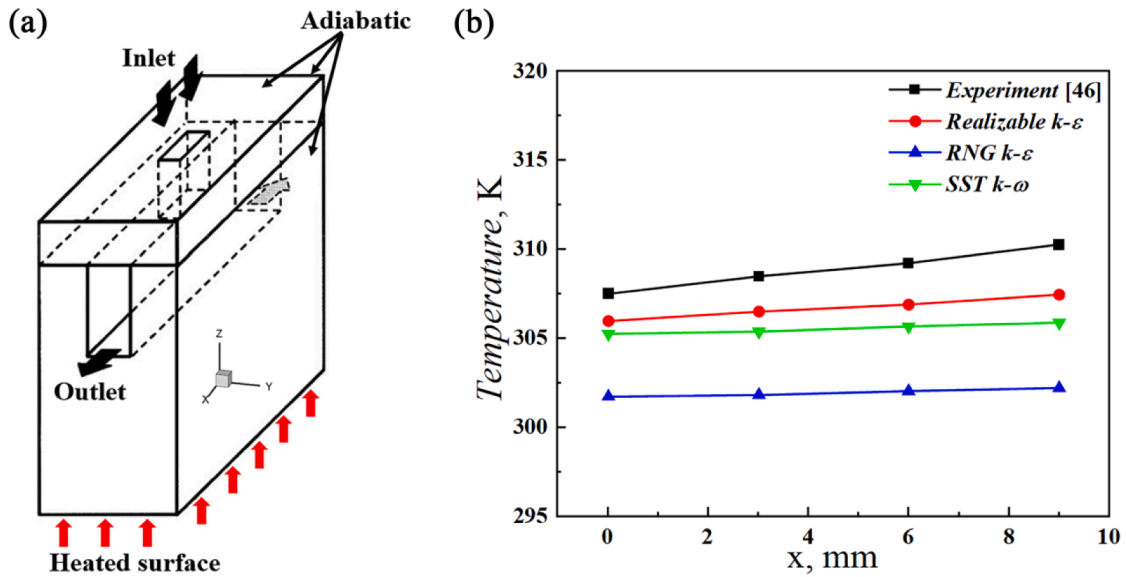
**Fig. 5.** (a) Diagram of the computational unit consisting of slot jet and microchannel; (b) Validation of turbulence models.

**Table 3**
Turbulence model verification.

|  | Position along x-axis, mm | 0 | 3 | 6 | 9 |
|---|---|---|---|---|---|
| Experiment [46] | Experimental value | 307.5 | 308.48 | 309.22 | 310.27 |
| Realizable k-ε | Calculated value | 305.97 | 306.5 | 306.9 | 307.46 |
|  | Relative error | 0.5% | 0.64% | 0.75% | 0.91% |
| RNG k-ε | Calculated value | 301.73 | 301.82 | 302.04 | 302.21 |
|  | Relative error | 1.9% | 2.16% | 2.32% | 2.6% |
| SST k-ω | Calculated value | 305.26 | 305.38 | 305.67 | 305.88 |
|  | Relative error | 0.73% | 1% | 1.15% | 1.41% |

solutions will be continuously optimized until the maximum generation number or the minimum criteria is fulfilled. In addition, the MOPSO was proposed by Coello et al. [51] on the basis of particle swarm algorithms (PSO), utilizing the grid-making technique and Pareto envelops to address multi-objective problems. Analogous to particle swarm algorithms, the motion of particles, i.e. solutions, is steered by their own individual optimal memory (the optimal position experienced by the particle) and the global best particle. Consequently, the particles will constantly change their state in the multidimensional search space until reaching the optimal state or exceeding the computational limit.

Additionally, as the surrogate model, the artificial neural network (ANN) is adopted to represent the relations between the optimization objectives and design variables. Firstly, based on the results of parametric analysis, the numerical test combinations are designed and calculated. The calculation results with structure parameters are later imported into the ANN for training, and the training results, i.e. trained surrogate model, will contain the relations between the optimization objectives and design variables. Then the optimization algorithms, i.e. MOPSO and MOGA, are utilized to optimize the trained surrogate model and the Pareto front will be acquired. Ultimately, the optimal compromise solution that meets the actual demand is obtained from the Pareto front by using the design-making algorithm. The optimization procedures are shown in Fig. 6.

### 2.7.2. Optimization objectives and design of artificial neural networks

In practical applications, the total pressure and the average heated surface temperature are the two most critical indicators to evaluate the comprehensive performance of the heat sink. The primary purpose of this work is to acquire the best structure parameters that simultaneously
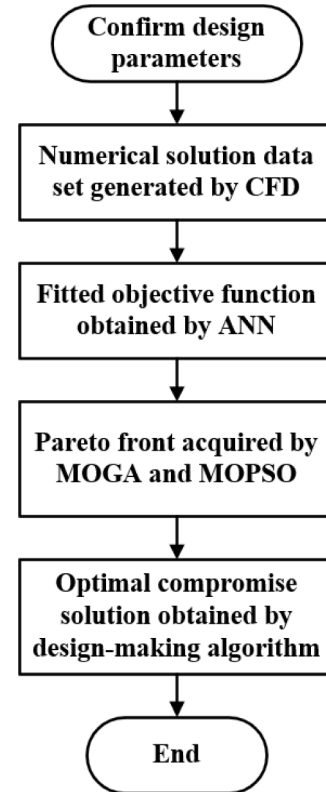


**Fig. 6.** Flow chart of structure parameter optimization.

minimize both the total pressure drop and average heated surface temperature. Therefore, two conflicting objectives are defined as follows:

$$J_1 = \overline{T}_{heat} \tag{16}$$

$$J_2 = \Delta P \tag{17}$$

where $\overline{T}_{heat}$ and $\Delta P$ are the average heated surface temperature and total pressure drop of the heat sink, respectively. As mentioned above, these two conflicting objectives will be optimized at the same time by using

the optimization slgorithm. Consequently, both $J_1$ and $J_2$ will continually decrease as the iteration proceeds until the termination criteria are reached.

To reduce the heavy workload of direct numerical simulation optimization, a total three-layer neural network based on error back propagation algorithm is utilized, in which the Tansig transfer function and Purelin transfer function are adopted for the hidden and output layer, respectively. Additionally, to ensure the training accuracy of the ANNs, all input data are normalized to the range of [0,1] and the proporation of data in the training, validation and test set are set up as 70%, 15% and 15%, respectively. Eqs. (18) present the correlations of normalized $J_1$ and $J_2$, where $w$ is the weight; $m$ is the number of hidden layer neurons; the subscript $i, j$ and $k$ represent the input, hidden and output layer, respectively.

$$J_1 \text{ or } J_2 = \sum_{j=1}^{m} w_{1j}\left(\frac{2}{1+e^{-2\left(\sum_{i=1}^{3} w_{ji}x_i + b_j\right)} - 1}\right) + b_k \quad (18)$$

Two commonly used evaluation indexes, i.e. mean square error $MSE$ and regression coefficient $R^2$, are adopted to assess the fitting performance of ANNs, shown in Eqs. (19) and Eqs. (20). The larger the $R^2$ and the smaller the $MSE$, the higher the accuracy of the ANNs.

$$MSE = \frac{1}{N}\sum_{i=1}^{n}\left(y_{i,ANN} - y_i\right)^2 \quad (19)$$

$$R^2 = 1 - \sum_{i=1}^{N}\frac{\left(y_{i,ANN} - y_i\right)^2}{y_i^2} \quad (20)$$

## 3. Results and discussion

### 3.1. Effects of the inlet and outlet branch passage inclination ratio

The suitable design of inlet and outlet branch passage inclination ratios ($H_{in,1}/H_{in,2}$ and $H_{out,1}/H_{out,2}$) is significant for the heat transfer and resistance characteristics, which directly affects the mass flow distribution among the heat transfer microchannels [30,31]. However, in most previous studies on SJIMHS, the same inclined tapering passages were used for the inlet and outlet branch passages without detailed parameters studies [52–54]. Fig. 7 depicts the temperature contour diagram of the heat transfer surface for different inclination ratios, where the same inclination ratio is used for the inlet and outlet branch passages ($H_{in,1}/H_{in,2} = H_{out,1}/H_{out,2}$). In addition, the channel unit width, channel width ratio and channel height are 2 mm, 0.6 and 1.5 mm respectively. It could be evidently seen that the low-temperature and high-temperature zones appear at intervals on the heat transfer surface, which are just positioned below the inlet and outlet branch passages, respectively. Due

to the scouring effect and relatively lower temperature, the cooling capability is better in the area below inlet branch passages and the corresponding temperature of the heat transfer surface is much lower [31]. As the inclination ratio increases, i.e. $H_{in/out,1}$ increases, the temperature non-uniformity increases slightly at the same time, which is different from our expectation that the variation of inclination ratio will have a large effect on the cooling capability.

Additionally, altering the inclination ratio has less impact on the mass flow distribution among the heat transfer channels and the mass flow distribution uniformity is poor, as illustrated in Fig. 8(b), which results in the uneven temperature distribution on the heat transfer surface. The observation of the flow distribution illustrates that the mass flow rate of the channels close to the heat sink inlet is smaller than that close to the heat sink outlet, which is similar to the numerical research by Zhou et al [30,31]. The first cause for this flow mal-distribution is that the inlet fluid splashes upward after impacting the bottom surface, resulting in a small velocity component along the positive z-axis near the heat sink inlet region. The upward splashing fluid is in the opposite direction of the jet, thus slowing the jet velocity along the negative z-axis, as demonstrated in Fig. 9(a). Comparing the red dashed boxes in Fig. 9(a), it is noticeable that the magnitude of the z component velocity along the negative direction of the z-axis is significantly smaller in the inlet region. The second reason is that more fluid tends to flow into the channels near the heat sink outlet where the lowest system pressure exists, as shown in Fig. 9(b).

Unlike the small effect on heat transfer characteristics, the variation in the inclination ratio has a large influence on pressure drop, as illustrated in Fig. 8(a). Since $H_{in/out,2}$ remains constant, the larger the inclination ratio, the larger the flow area of the inlet and outlet branch passage, and thus the passage resistance loss decreases significantly, which is mainly reflected in the obvious reduction of $\Delta P_1$ and $\Delta P_3$.

Although the pressure drop can be significantly lowered by increasing the branch passage inclination ratio, the flow resistance is still large, exceeding 100 kPa, and the temperature distribution is uneven. To further optimize the heat sink cooling capability and resistance performance, the structure parameters, i.e. $H_{in,2}$ and $H_{out,2}$, were investigated separately, which were seldom investigated in previous studies. According to the above study, the heat sink with $H_{in/out,1} = 6$ stands out in flow resistance reduction, hence $H_{in/out,1} = 6$ is adopted in subsequent structural parameter studies. Fig. 10 shows the temperature contour diagram of heat transfer surface for different $H_{in,2}$ or $H_{out,2}$, in which the numbers labeled on the figure from left to right represent $H_{in,1}$, $H_{in,2}$, $H_{out,2}$ and $H_{out,1}$. When comparing the figure laterally, e.g. comparing ABC, DEF or GHI, the outlet branch passage inclination ratio remains constant, and temperature distribution uniformity of the heat transfer surface is worse as the inlet passage inclination ratio is smaller, i.e.
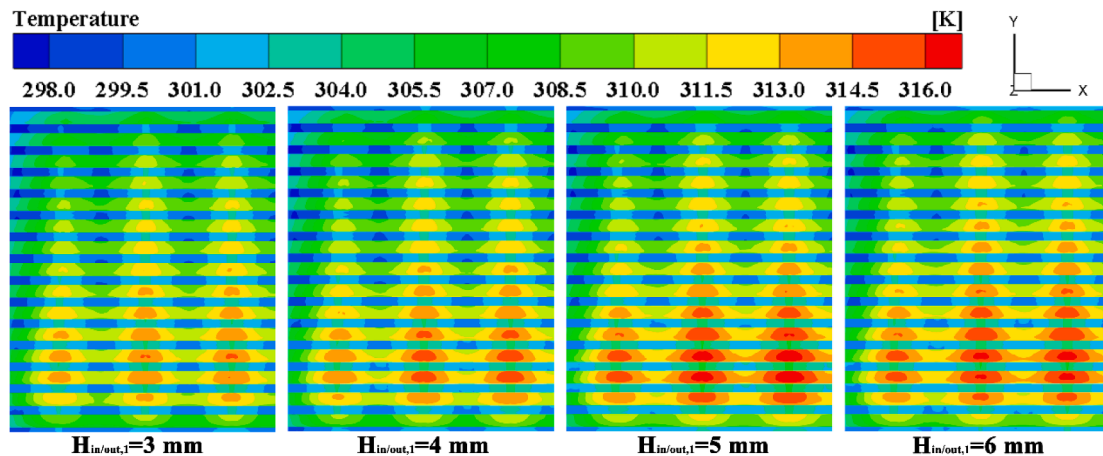


**Fig. 7.** The contour diagram of heat transfer surface temperature for different inlet/outlet passage inclination ($H_{in/out,2} = 0.5$ mm, $q = 200$ W/cm$^2$, $V_{in} = 6$ m/s).
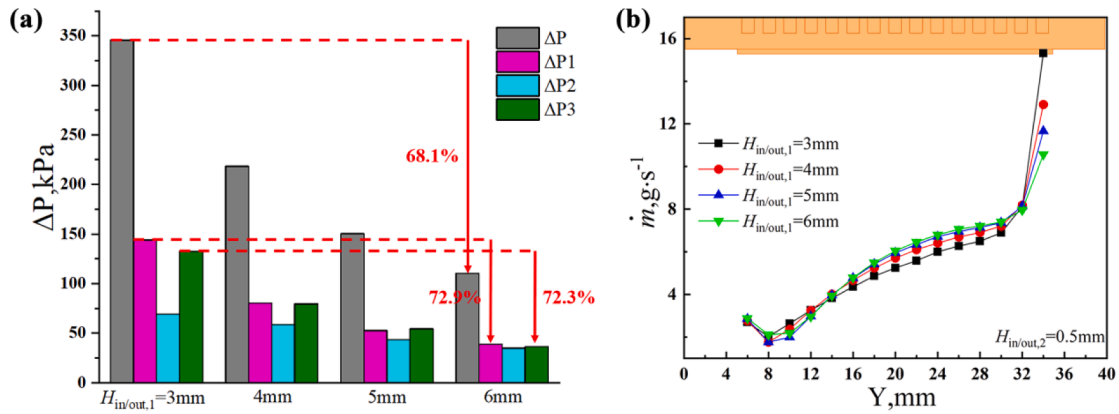
**Fig. 8.** Effects of the inlet/outlet passage inclination: (a) Pressure drop comparison; (b) Flow distribution among heat transfer microchannels.
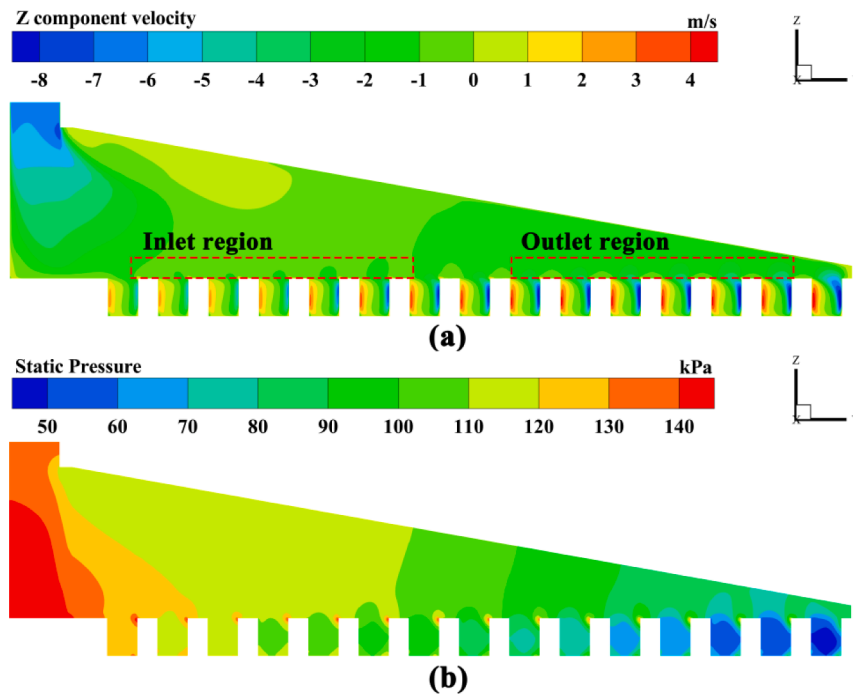


**Fig. 9.** The contour diagram of inlet branch passages: (a) Z component velocity; (b) Static pressure ($H_{in/out,1} = 6$ mm).

larger $H_{in,2}$. The main reasons for the uneven temperature distribution are the uneven mass flow distribution among the heat transfer channels and the interval arrangement of inlet and outlet branch passages, which can be confirmed in Fig. 11(b). It should be noted that the symbols presented in the legend of Fig. 10, i.e. A, B, C, etc., correspond to that of Fig. 10. However, when comparing the figure vertically, e.g. comparing ADG, BEH and CFI, the inlet branch passage inclination ratio remains constant, and the temperature distribution uniformity is better as the outlet branch passage inclination ratio is smaller, i.e. larger $H_{out,2}$. As presented in Fig. 11(b), the mass flow distribution among the heat transfer channels becomes more uniform as the $H_{out,2}$ increases, and the heat sink G with minimum $H_{in,2}$ and maximum $H_{out,2}$ shows the optimal uniformity of the mass flow distribution and the best cooling capability.

In addition, Fig. 12 compares the streamline distribution diagrams corresponding to the three heat sink structures A, C and G in Fig. 10. The heat sink A is the original structure, which has the smallest $H_{in,2}$ and $H_{out,2}$. The heat sink C corresponds to the largest $H_{in,2}$ and the smallest $H_{out,2}$, while the heat sink G corresponds to the smallest $H_{in,2}$ and the largest $H_{out,2}$. Observing the streamline distribution, it can be seen obviously that for heat sinks A and C, the streamlines are much denser

close to the heat sink outlet while less near the inlet region, which is consistent with the mass flow distribution in Fig. 11(b). The main causes are attributed to liquid splashing and pressure gradients that have been analyzed above. Nevertheless, the streamline distribution of heat sink A is much more uniform than heat sink C and the heat sink G has the most uniform distribution, which indicates that the larger inlet branch passage inclination ratio and smaller outlet branch passage inclination ratio can suppress upward splashing of fluid and improve the pressure distribution.

Consequently, it can be found that the variations in the inlet and outlet branch passage inclination ratios have almost opposite effects on the cooling capability, which explains the slight influence of inclination ratio variation when the inlet and outlet branch passage inclination ratios are the same. Additionally, a relatively low pressure drop is achieved by heat sink G, as illustrated in Fig. 11(a). Therefore, the inlet and outlet passage parameters are maintained the same as the heat sink G in the subsequent structural parameters research.
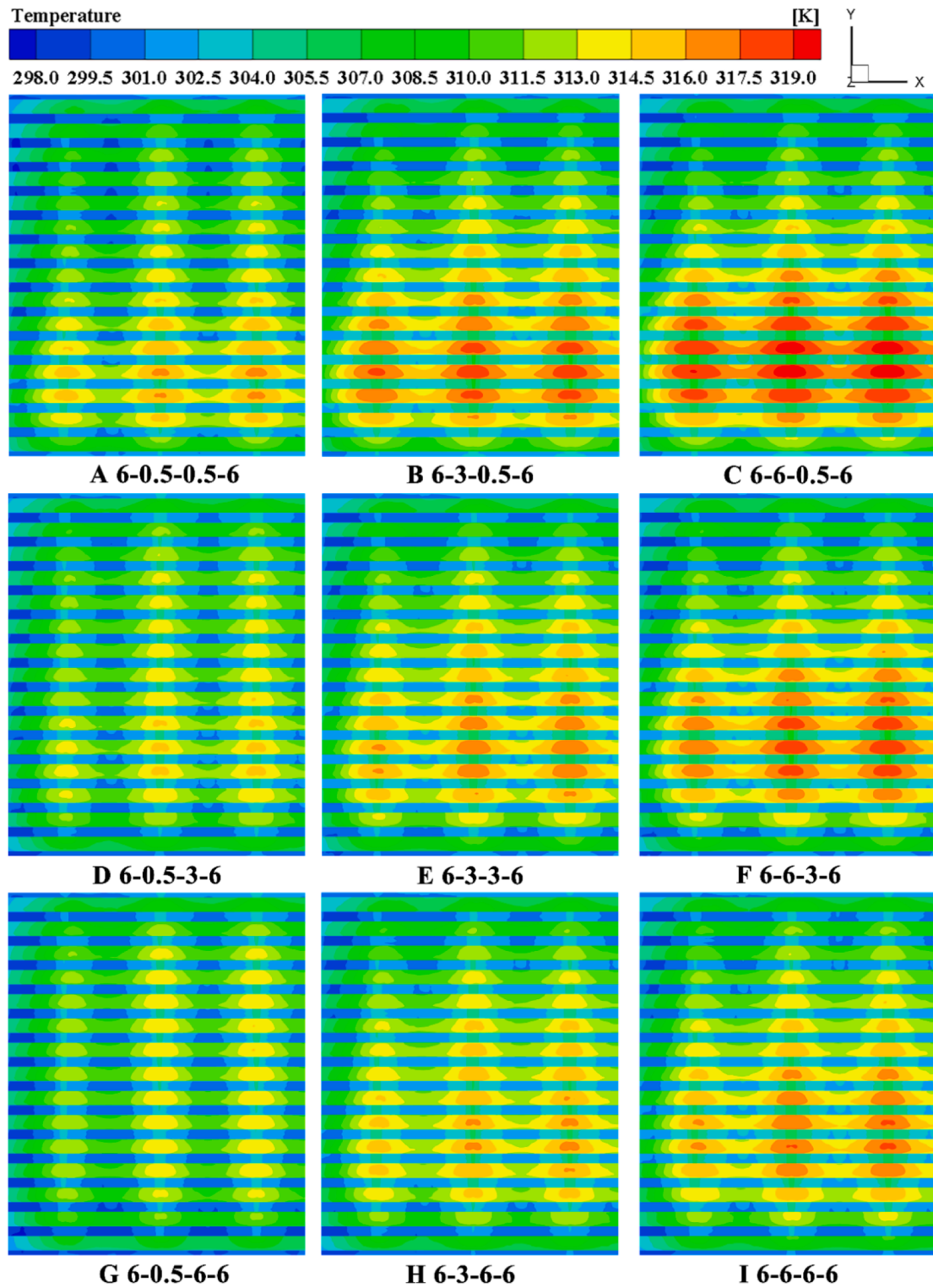
**Fig. 10.** The contour diagram of heat transfer surface temperature for different inlet and outlet passage inclination ($q = 200$ W/cm$^2$, $V_{in} = 6$ m/s).

## 3.2. Effect of channel unit width

To evaluate the impact of channel unit width ($W_1$) variation on cooling capability and flow resistance characteristics of the hybrid scheme, the variations of the average heated surface temperature ($\overline{T}_{heat}$), the total pressure drop ($\Delta P$), the average heat transfer coefficient ($\overline{h}$) and the heat transfer area of the channels ($S_t$) for different channel unit width are given in Fig. 13. On the whole, with the increase of $W_1$, the

$\overline{T}_{heat}$ increases gradually and the $\overline{h}$ reduces progressively, which indicate that the increase of $W_1$ deteriorates the cooling capability. Analysis of the variation in $W_1$ reveals that the decreased heat transfer area deteriorates the cooling performance. As depicted in Fig. 13 (d), when the heat sink width is constant, the increase of $W_1$ will lead to the decrease in the channel numbers, which results in a decrease in the channel heat transfer area. Fig. 13(c) illustrates the change of total pressure drop with the variation of $W_1$. Unlike the heat transfer performance, when the
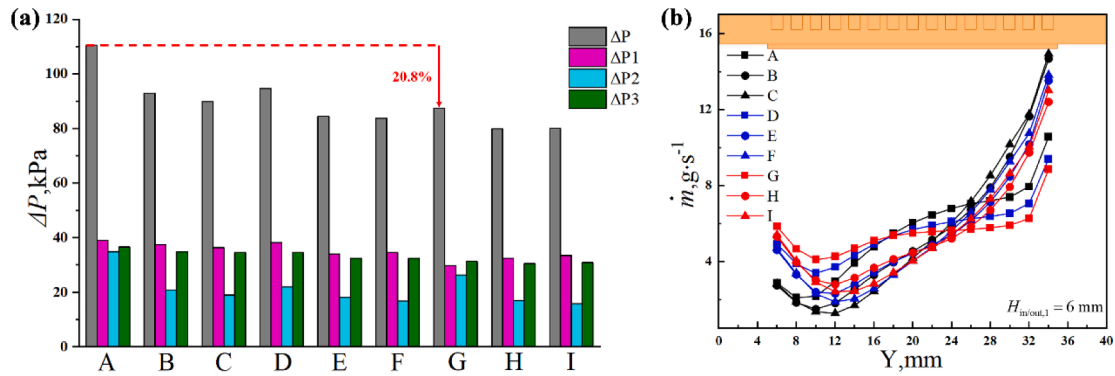
**Fig. 11.** Effects of the inlet and outlet passage inclination: (a) Pressure drop comparison; (b) Flow distribution among heat transfer microchannels.
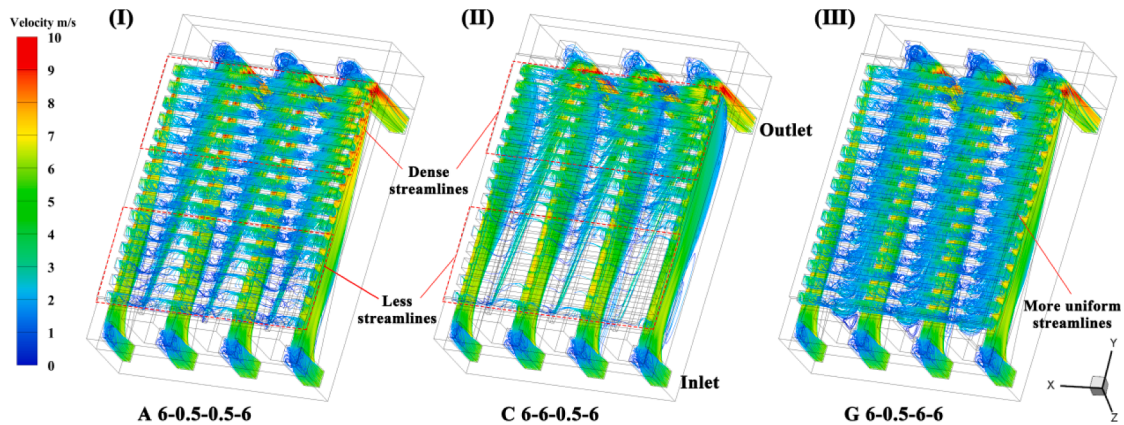


**Fig. 12.** Streamlines distribution for different inlet and outlet passage inclination: (I) 6-0.5-0.5-6 corresponding to A in Fig. 10; (II) 6-6-0.5-6 corresponding to C in Fig. 10; (III) 6-0.5-6-6 corresponding to G in Fig. 10.

channel height ($H_3$) or channel width ratio ($\varphi$) is different, then changing the channel unit width has a different impact on the flow resistance characteristics. For example, when $H_3$ and $\varphi$ are small, i.e. $H_3 = 0.5$ mm and $\varphi = 0.4$, then the $\Delta P$ decreases with the increase of $W_1$, and the $\Delta P$ reduces by about 10% when the maximum channel unit width ($W_1 = 3$ mm) is adopted compared to the minimum channel unit width ($W_1 = 1$ mm). However, when a large $H_3$ or $\varphi$ is used, i.e. $H_3 = 2.5$ mm or $\varphi = 0.8$, the total pressure drop fluctuates or increases with the increasement of $W_1$. To analyze the causes of this anomaly, Fig. 14 shows the velocity contours and vector diagrams of the inlet branch passage slice corresponding to different channel unit width. Comparing Fig. 14(a), (b) and (c), it can be obviously found that the velocity is relatively higher in the heat transfer channel when $H_3$ and $\varphi$ is small, which may lead to a relatively large on-way resistance along the heat transfer channel. Additionally, with the reduction of $H_3$ and $\varphi$, the consequent shorter jet impact distance and higher jet velocity will result in greater jet impact losses. Therefore, for small channel height, as the channel unit width increases, the reduction in channel sidewall area reduces the on-way resistance loss and lowers the pressure drop.

As delineated in Fig. 14(a), a clockwise vortex structure is formed in all channels when the $H_3$ is small. However, when the $H_3$ is large and the $W_1$ is small, the fluid flushes the channel bottom surface almost vertically, and does not form a clockwise vortex in the channels, which can be observed in Fig. 14(c). The same phenomenon was also found in Refs [29], and the main reason may be that the channel aspect ratio is too large and the velocity becomes smaller at the channel corner, which is not conducive to the formation of a vortex structure. As the channel unit width increases, the channel aspect ratio decreases and vortex structures are formed in the heat transfer channels, which strengthens the fluid disturbance and lead to deterioration of the resistance performance.

Consequently, for the heat sink with a large channel height, as the channel unit width increases, the effect of viscous dissipation caused by vortex structure is greater than the effect of reduced on-way resistance losses due to the reduced channel area, so the pressure drop shows a gradually increasing trend. As for the case with a large channel width ratio, when the channel unit width is small, a single clockwise vortex structure is formed in the heat transfer channels. However, as the channel unit width increases, the vortex structure is continuously stretched and forms multiple vortex structures, resulting in more complex flow in the channel. Therefore, under the joint influence of sidewall area and vortex structure, the heat sink pressure drop reduces marginally with the increase of channel unit width and then increases marginally.

### 3.3. Effect of the channel width ratio and channel height

Fig. 15 presents the effect of channel height ($H_3$) and channel width ratio ($\varphi$) variation on cooling capability and resistance characteristics at $W_1 = 2$mm. As illustrated in Fig. 15 (a) and (c), with the increase of $\varphi$, the $\overline{T}_{heat}$ increases significantly, and the $\Delta P$ and $\overline{h}$ decrease considerably at the same time. It suggests that larger channel width ratio can improve the resistance performance while causing deterioration in heat transfer performance. As previously analyzed, the larger the channel width ratio, the smaller the jet velocity and channel velocity, which will reduce the jet impact loss and on-way resistance along the channel, thus improving the resistance performance. Nevertheless, the reduction of jet velocity and channel velocity will thicken the flow boundary layer and thus weakens the convective heat transfer performance. In addition, when the channel width ratio is relatively small, the $\Delta P$ corresponding to different channel heights varies obviously. However, as the channel
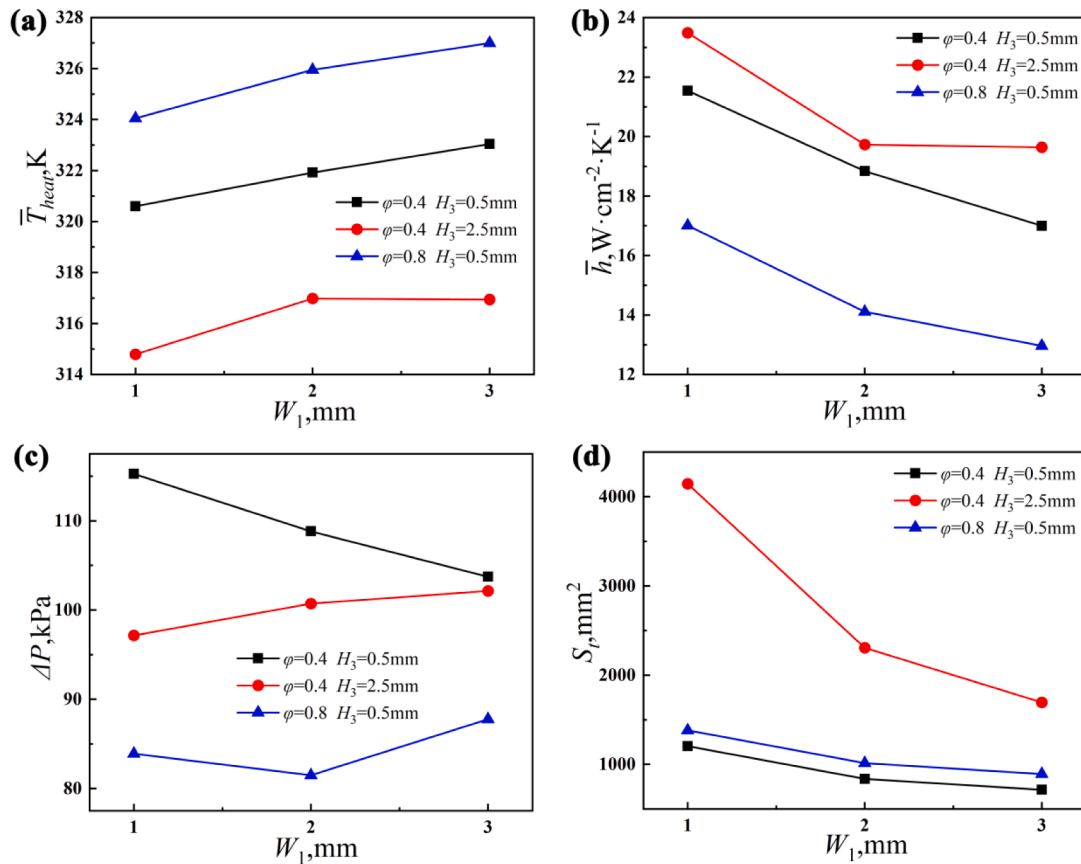
**Fig. 13.** Effects of the channel unit width: (a) The average heated surface temperature; (b) The average heat transfer coefficient; (c) The total pressure drop; (d) The heat transfer area of the channels.

width ratio increases, the pressure drop difference decreases progressively. The primary cause for this phenomenon is the same as the above analysis that the increased channel width ratio reduces the jet velocity and channel velocity. As a result, when the flow velocity decreases, the difference in on-way resistance and jet impact loss due to the change of channel height diminishes simultaneously.

Observing Fig. 15(d), the $\overline{T}_{heat}$ decreases progressively as the channel height increases. As depicted in Fig. 13(d), when the channel unit width and channel width ratio remain constant, the heat transfer area of the maximum channel height is nearly 2 or 3 times larger than that of the minimum channel height. Consequently, the improved heat transfer performance because of the increased heat transfer area results in a lower heated surface temperature. However, the downtrend of $\overline{T}_{heat}$ is decelerated with the increase of $H_3$, especially obvious for larger $\varphi$. The large $\varphi$ and $H_3$ will reduce the jet and channel velocity, so the enhanced heat transfer effect due to the enlarged heat transfer area will be weakened. Unlike the variation trend of $\overline{T}_{heat}$, the $\overline{h}$ increases first and then decreases with the increase of channel height, which indicates that the change trend of the average heat transfer surface temperature does not match with variation trend of $\overline{T}_{heat}$. Fig. 16 presents the temperature contour diagram of heat transfer surface and heated surface for different channel heights. Clearly, the temperature distribution and temperature variation trend of the heat transfer surface are quite different from that of the heated surface. The primary cause is that the change of channel height will affect the distance from the heat transfer surface to the heated surface, which will impact the thermal resistance and thus change the temperature differential between the heat transfer surface and heated surface. For example, when the $H_3$ is low, because of the short jet impact distance, the jet scouring cooling performance is better and thus the heat transfer surface temperature is lower. Nevertheless,

the distance from heat transfer surface to heated surface will be extended due to the reduction in channel height. Based on the Fourier's law of heat conduction, the temperature differential between heat transfer surface and heated surface will increase when the heat flux is constant. Consequently, the temperature variation trend of the heat transfer surface will not reflect that of the heated surface when the channel height is different. Similar to the study by Deng et al. [29], they found that with the decrease of base thickness, the thermal resistance will reduce firstly. However, when the base is very thin, the lateral heat transfer in X and Y directions will be weakened, resulting in a bigger thermal resistance. In practical applications, the heat source and heated surface will be closely fitted, hence the heated surface temperature truly reflects the temperature of the electronics. Therefore, the $\overline{T}_{heat}$ is chosen as the optimization target to assess the cooling capability in the subsequent optimization.

When the channel height is lower than 1.5 mm, as the channel height increases, the heat transfer enhanced effect brought by the enlarged heat transfer area is greater than the weakening effect due to the extended jet impact distance, so the average heat transfer surface temperature decreases and thus $\overline{h}$ increases. However, as the channel height continues to increase, the weakening effect takes the dominant role and thus $\overline{h}$ decreases. Unlike the significant impact of changing the $\varphi$ on resistance characteristics, changing the channel height has a relatively little effect. The total pressure drop varies more obviously with the channel height at a small $\varphi$, while the effect of channel height variation diminishes as the $\varphi$ increases, as depicted in Fig. 15(f).
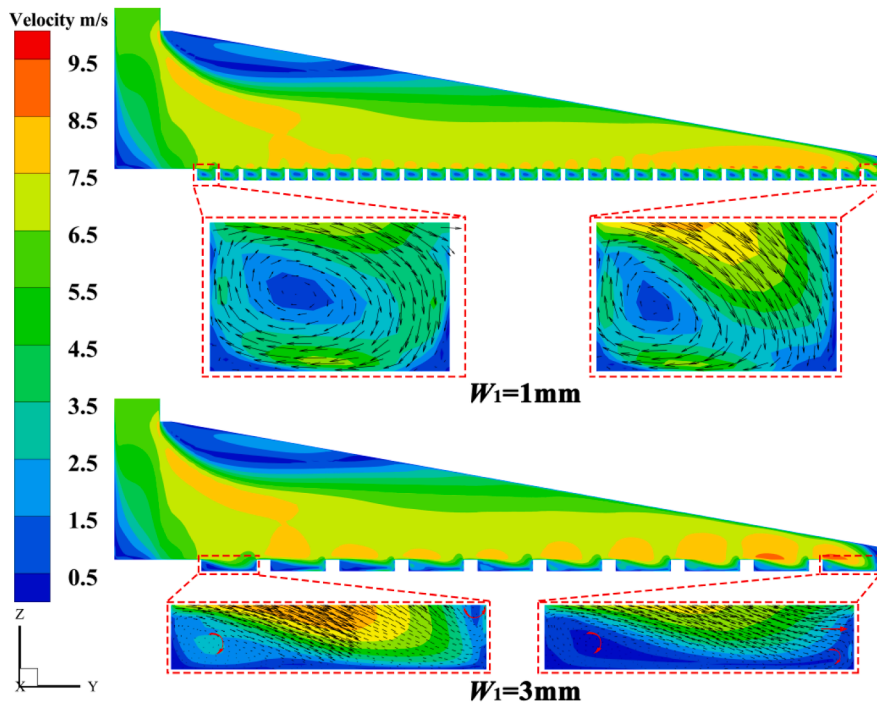
### 3.4. Results of structure parameters optimization

#### 3.4.1. Analysis of ANNs

According to the parameters analysis, the structure parameters of the
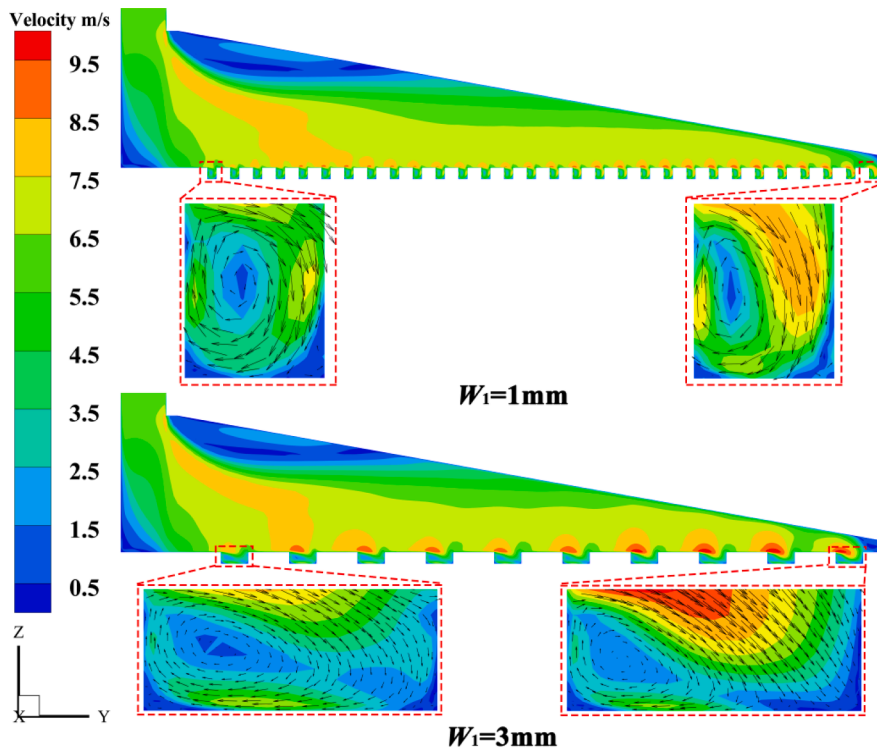
**Fig. 14.** Contour and vector of velocity magnitude for different channel unit width: (a) $\varphi = 0.4, H_3 = 0.5$ mm; (b) $\varphi = 0.8$, $H_3 = 0.5$ mm; (c) $\varphi = 0.4$, $H_3 = 2.5$ mm.

inlet and outlet branch passage, the channel unit width ($W_1$), the channel width ratio ($\varphi$) and the channel height ($H_3$) have noticeable effects on heat sink cooling performance. Considering the computational efficiency and the almost monotonic effect of the variation of inlet and

outlet branch passage parameters on heat transfer and resistance characteristics, the branch structure parameters of heat sink G in Section 3.1 are selected as the optimal solution. As shown in Tables 4, 3, 5 and 5 levels are selected for $W_1$, $\varphi$ and $H_3$, respectively. A total of 75 numerical
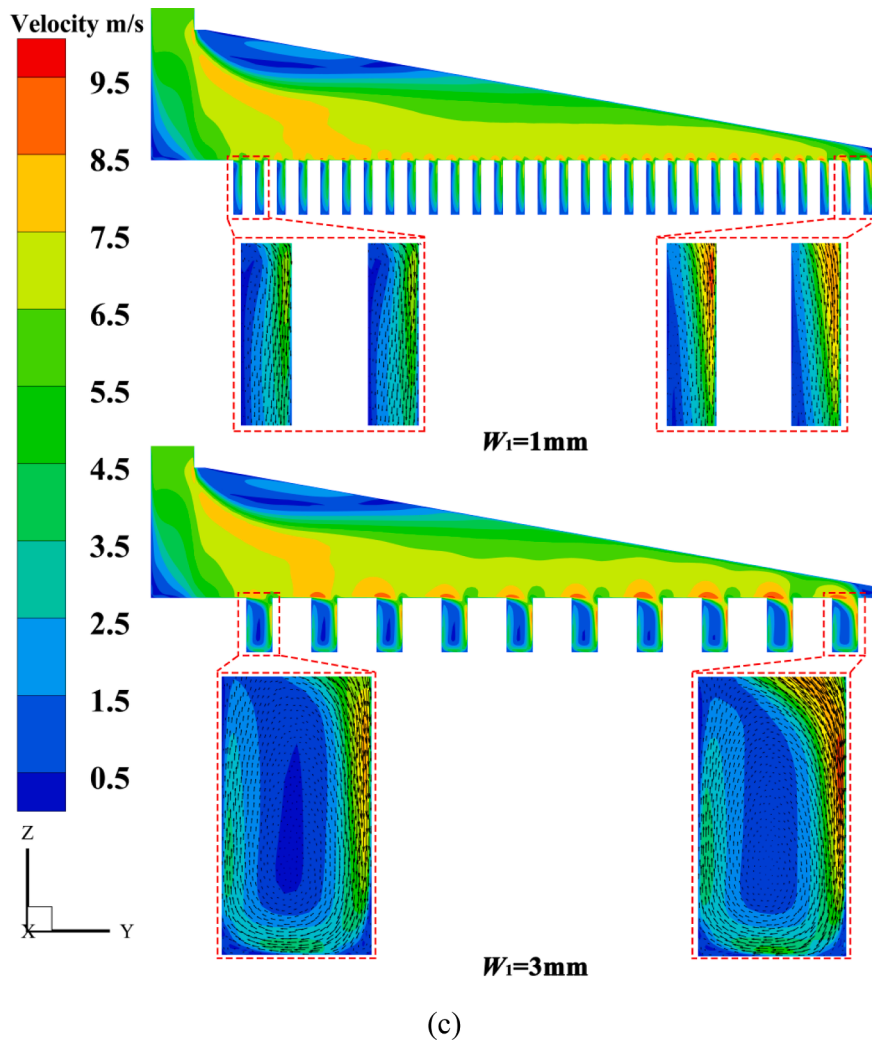
$W_1=1mm$

$W_1=3mm$
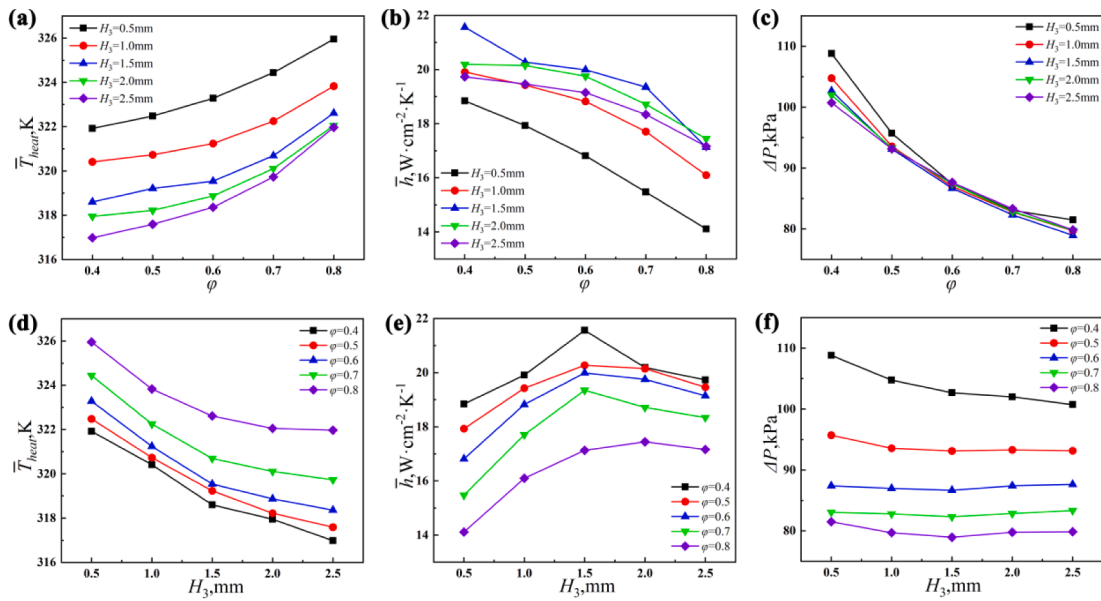
(c)

**Fig. 14.** (*continued*).



**Fig. 15.** Effects of the channel width ratio: (a) The average heated surface temperature; (b) The average heat transfer coefficient; (c) The total pressure drop; and effects of the channel height: (d) The average heated surface temperature; (e) The average heat transfer coefficient; (f) The total pressure drop.
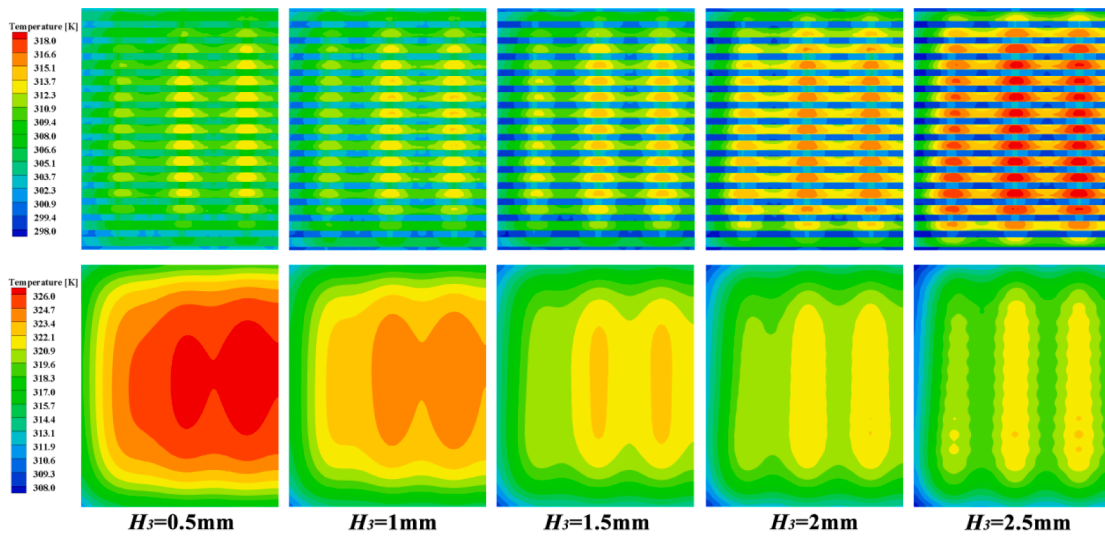
**Fig. 16.** The temperature contour diagram of heat transfer surface and heated surface at different channel height.

**Table 4**
Design parameters for numerical simulations.

| Design parameters | Values |
|---|---|
| $W_1$, mm | 1, 2, 3 |
| $\varphi$ | 0.4, 0.5, 0.6, 0.7, 0.8 |
| $H_3$, mm | 0.5, 1, 1.5, 2, 2.5 |

**Table 5**
Neuron independence verification for $J_1$ and $J_2$.

| Number of neurons | $J_1 = \overline{T}_{heat}$ | | $J_2 = \Delta P$ | |
|---|---|---|---|---|
| | MSE | $R^2$ | MSE | $R^2$ |
| 1 | 1.6004 | 0.99977 | 28.527 | 0.95209 |
| 2 | 7.7781 | 0.99888 | 20.753 | 0.96293 |
| 3 | 2.8722 | 0.999582 | 21.069 | 0.96574 |
| 4 | 1.5004 | 0.999782 | 89.714 | 0.84614 |
| 5 | 1.1261 | 0.999838 | 18.227 | 0.96757 |
| 6 | 1.5834 | 0.999771 | 37.664 | 0.93499 |
| 7 | 1.5938 | 0.999767 | 12.047 | 0.98144 |
| 8 | 3.5493 | 0.999489 | 12.550 | 0.97726 |
| 9 | 1.6078 | 0.999766 | 15.181 | 0.97180 |
| 10 | 13.4879 | 0.998029 | 19.775 | 0.96334 |
| 11 | 1.9851 | 0.999709 | 18.451 | 0.96938 |
| 12 | 1.6306 | 0.999761 | 38.464 | 0.93063 |
| 13 | 5.4030 | 0.999210 | 23.026 | 0.95886 |
| 14 | 2.8736 | 0.999585 | 26.508 | 0.95097 |
| 15 | 7.1126 | 0.998967 | 33.267 | 0.93845 |

simulations are implemented by Fluent 16.0, and the numerical results will be adopted as the data input of ANNs.

In the optimization procedure, the accuracy of the fit function obtained by ANNs is significant affected by the number of hidden layer neurons. Too few neurons cannot be able to capture all the data features and lead to underfitting, while too many neurons will lead to overfitting. Both situations will deteriorate the overall fitting performance of ANNs. In order to fully utilize the sample data and avoid overfitting or underfitting, the number of hidden layer neurons was tested in this section. Table 5 shows the fitting performance of ANNs for different hidden layer neuron numbers. According to the test results, the optimal number of hidden layer neurons for two conflicting objective functions, i.e. $J_1 = \overline{T}_{heat}$ and $J_2 = \Delta P$, is 5 and 7, respectively. Additionally, the numerical simulation results obtained by CFD are compared with the predicted values of ANNs to further verify the fitting accuracy. The predicted values of ANNs match well with the numerical simulation

values, as presented in Fig. 17, and the maximum errors are 0.6% and 6.17%, respectively.

Although the maximum error of the trained model in pressure drop is more than 6%, it exists only in a few cases. By comparing the predicted and calculated values for 75 data points, it can be found that the relative error exceeds 5% for only two points and is less than 3.5% for 90% of the data sets. In addition, the structural parameters corresponding to the points with maximum relative errors were also checked, i.e. $W_1 = 3$, $\varphi = 0.8$ and $H_3 = 0.5$. These values are located at the edges of the parameter variation range, which usually results in extreme values for a certain performance, i.e. heat transfer or flow resistance. In this work, the maximum relative error point corresponds to the highest $\overline{T}_{heat}$ and moderate $\Delta P$, i.e. $\overline{T}_{heat} = 325.57$K and $\Delta P = 82.35$kPa. When performing multi-objective optimization, these points are usually excluded as dominant solutions. Consequently, the trained ANNs can be confirmed to have relatively high accuracy and can be adopted for subsequent optimization research.

*3.4.2. Multi-objective optimization results analysis*

As mentioned above, the multi-objective optimization problem could be expressed as follows:

Minimization: $J_1 = f_1(W_1, \varphi, H_3)$ and $J_2 = f_2(W_1, \varphi, H_3)$.

Subject to: $W_1 \in [1, 3]$, $\varphi_1 \in [0.4, 0.8]$ and $H_3 \in [0.5, 2.5]$.

To optimize the two conflicting objectives, the MOGA and MOPSO are adopted. The more detailed information about MOGA and MOPSO can be found in Refs [50] and [51]. In addition, some working parameters of two algorithms are demonstrated in Table 6. Fig. 18(a) illustrates the comparison of the Pareto front of MOGA and MOPSO, both of which contain 40 non-inferior solutions. In addition, all points that located on the Pareto front are globally optimal and there is no difference in superiority between individual points. Moving along the Pareto front, as one optimization objective improves, the other optimization objective is bound to deteriorate. As illustrated in Fig. 18(a), the Pareto front derived by MOPSO almost coincides with that of MOGA, which indicates that the optimal solutions obtained by MOPSO or MOGA are non-inferior solutions and verifies the effectiveness of both algorithms. Nevertheless, the Pareto front obtained by MOPSO has a smaller range of objective functions, indicating that the Pareto front obtained by MOGA may provide more alternative solutions in practical applications. Consequently, the optimal compromise solution is selected from MOGA in the subsequent study, while the optimal $\overline{T}_{heat}$ is varied from 316.7 K to 322 K and the optimal $\Delta P$ is varied from 96.1 kPa to 78.6 kPa.
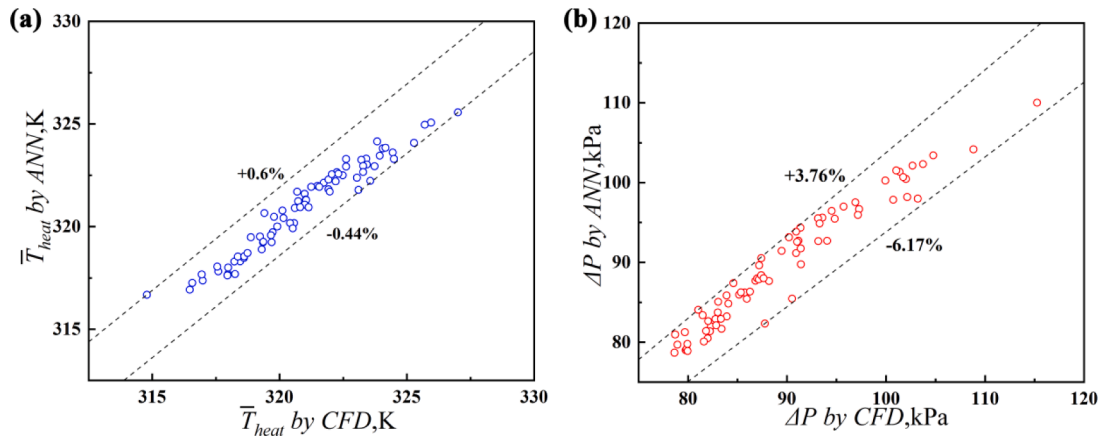
**Fig. 17.** Comparison of CFD values with ANN predicted values: (a) $J_1 = \overline{T}_{heat}$; (b) $J_2 = \Delta P$.

**Table 6**
Parameter settings of MOPSO and MOGA.

| MOPSO | Population size | 200 |
|---|---|---|
| | Repository size | 40 |
| | Iteration | 200 |
| | Grid | 7 |
| | | |
| MOGA | Population size | 200 |
| | Pareto fraction | 0.2 |
| | Generation | 200 |
| | Migration fraction | 0.2 |
| | Crossover fraction | 0.8 |
| | Function tolerance | $5 \times 10^{-5}$ |

### 3.4.3. Optimal compromise solution selection and comparison

Although the non-inferior solution set is obtained, it is usually necessary to obtain the optimal compromise solution in practical applications. However, as mentioned above, each point located on the Pareto front is a non-inferior solution, thus we cannot randomly choose a point from the front as the optimal solution. Nevertheless, it can be found that further decrease of the objective function is more difficult at both ends of the Pareto front, indicating that a solution with optimal compromise performance should exist between the endpoints. As a result, a classic decision-making algorithm, i.e. TOPSIS, is adopted in this work to search the optimal compromise solution. The main tenet of TOPSIS is that the distance between the optimal compromise solution and the ideal worst solution, i.e. imaginary solution with the highest $\overline{T}_{heat}$ and $\Delta P$, should be the longest, and the distance between the optimal compromise solution and the ideal optimal solution, i.e. imag-

inary solution with the lowest $\overline{T}_{heat}$ and $\Delta P$, should be the shortest. Moreover, detailed information about TOPSIS can be found in Refs [55]. In addition, the two optimization objectives are considered equally important, and an equal weighting factor, i.e. $w_{\overline{T}_{heat}} = w_{\Delta P} = 0.5$, is given to both optimization objectives according to the literature [55]. It should be emphasized that the weighting factor can be adjusted according to the application to acquire the optimal compromise solution satisfying practical requirements.

Fig. 18(b) shows the relative closeness values to the ideal optimal solution, which vary from 0.44 to 0.65. The solutions at the Pareto front endpoints, e.g. point A and B, obtain lower ranking scores, which implies that merely improving one objective function will result in a reduction in overall performance. Consequently, point C with the highest relative closeness value is chosen as the optimal compromise solution. Table 7 lists the corresponding structure parameters of points A, B and C. To assess the decision performance of TOPSIS, the optimized objective values of point A, B and C are compared: the $\overline{T}_{heat}$ minimization, the $\Delta P$ minimization and the optimal compromise solution. As illustrated in Fig. 19, compared with $\overline{T}_{heat}$ minimization, $\Delta P$ of the optimal

**Table 7**
Geometrical parameters of different solutions.

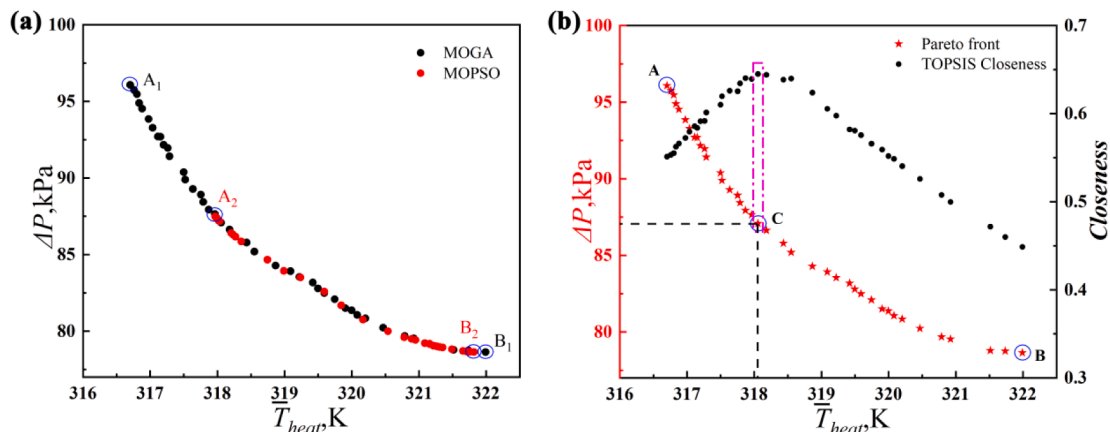| Solutions | Geometrical parameters | | |
|---|---|---|---|
| | $W_1$, mm | $\varphi$ | $H_3$, mm |
| A, $\overline{T}_{heat}$ minimization | 1 | 0.4 | 2.45 |
| B, $\Delta P$ minimization | 2.93 | 0.8 | 2.36 |
| C, TOPSIS | 1.03 | 0.58 | 2.44 |



**Fig. 18.** Distribution of Pareto fronts: (a) Comparison of the Pareto front of MOGA and MOPSO; (b) The Pareto front of MOGA and variation in relative closeness.

compromise solution can be reduced by 9 kPa with an increase of 1.4 K in $\overline{T}_{heat}$. Additionally, compared with $\Delta P$ minimization, even though $\Delta P$ increase by 8.4 kPa, $\overline{T}_{heat}$ can be reduced by 3.9 K. Therefore, the optimal compromise solution obtained by TOPSIS algorithm can significantly reduce the power consumption without increasing the average temperature significantly.

To further verify the accuracy of the ANNs model, three solutions on the Pareto front, i.e. the optimal solution C, endpoints A and B, have been modeled and calculated by CFD. As shown in Table 8, under the same working condition, i.e. $u_{in} = 6\text{m/s}$ and $q = 200\text{W/cm}^2$, the numerical values of CFD are basically the same as the predicted values of ANNs and the relative error is small, which further confirms the validity of the ANNs.

### 3.4.4. Optimal heat sink performance under different working conditions

With the purpose of improving optimization efficiency, the optimal compromise solution is achieved under a fixed inlet velocity and heat flux by combining artificial neural network training and multi-objective optimization algorithm. In practical situation, the variation of the inlet velocity ($u_{in}$), heat flux ($q$) and inlet temperature ($T_{in}$) also have significant impacts on the heat sink performance. In this section, the comprehensive thermal-hydraulic characteristics of the optimal compromise heat sink ($W_1 = 1.03$ mm, $\varphi = 0.58$ and $H_3 = 2.44$ mm) is investigated under different working conditions.

Fig. 20 (a)-(c) depicts the influence of heat flux variation on cooling capability and resistance characteristics at. With the increase of heat flux, the $\overline{T}_{heat}$ also increases linearly. When the heat flux is small, the $\overline{T}_{heat}$ corresponding to different inlet velocities is relatively close. Nevertheless, when the heat flux is close to, the $\overline{T}_{heat}$ corresponding to different inlet velocities differs greatly, and the $\overline{T}_{heat}$ corresponding to 6 m/s is nearly 25 °C lower than that corresponding to 1.5 m/s. Unlike the significant effect on, changing the heat flux has a small effect on the $\Delta P$ and $\overline{h}$. A similar phenomenon was also found by Deng et al. [29] in their experimental research. The main reason is that the heat flux variation has little influence on the thermophysical properties of water in single-phase heat transfer zone. In addition, the maximum and average temperature of the heated surface does not exceed 73 °C and 67 °C, respectively, and the $\Delta P$ is only 5.7 kPa, when the inlet velocity is 1.5 m/s and the heat flux is.

Fig. 20 (d)-(f) delineates the impact of the inlet velocity and inlet temperature variation on cooling capability and resistance characteristics at. With the increase of inlet velocity, the $\overline{T}_{heat}$ decreases significantly, and the $\Delta P$ and $\overline{h}$ increase simultaneously. Similar to our earlier experimental research [42], in single-phase convection heat transfer
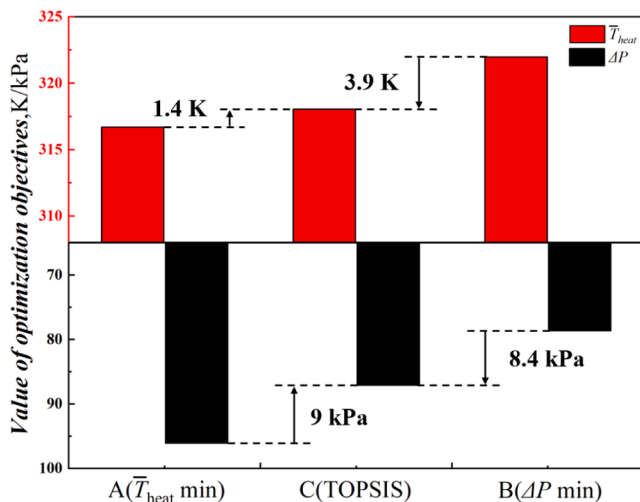
**Table 8**
Verification of the solutions on the Pareto front.

| Solutions | Objectives | Predicted value by ANN | Calculated value by CFD | Relative error |
|---|---|---|---|---|
| A, $\overline{T}_{heat}$ minimization | $\overline{T}_{heat}$, K | 316.7 | 316 | 0.22% |
| | $\Delta P$, kPa | 96.1 | 96.4 | 0.31% |
| B, $\Delta P$ minimization | $\overline{T}_{heat}$, K | 322 | 323.2 | 0.37% |
| | $\Delta P$, kPa | 78.7 | 79.3 | 0.76% |
| C, TOPSIS | $\overline{T}_{heat}$, K | 318.1 | 318.5 | 0.13% |
| | $\Delta P$, kPa | 87.1 | 85.4 | 1.99% |

zone, the increase of mass flow rate is the most effective way to enhance the cooling capability, but it will lead to an exponential increase in the total pressure drop. Additionally, when the inlet velocity is constant, the differential of $\overline{T}_{heat}$ corresponding to different inlet temperature is approximately equal to the inlet temperature difference, and the variation of the inlet temperature has little influence on the $\Delta P$ and $\overline{h}$.

## 4. Conclusion

To alleviate the drawbacks of traditional microchannel cooling and jet impingement/microchannel cooling, a novel slot jet impingement/microchannel heat sink with discharge manifold is proposed in this study. To examine the impact of the geometrical parameters on heat transfer and resistance characteristics, a 3-D numerical simulation was employed to one-half of the hybrid heat sink model. By combining CFD with neural network training, predictive models of the relationship between the two objectives, i.e. $\overline{T}_{heat}$ and $\Delta P$, and structural parameters were obtained with appropriate computational cost. Two multi-objective optimization algorithms, i.e. MOPSO and MOGA, are adopted to offer a credible Pareto front. Ultimately, the optimal compromise solution was selected from the Pareto front by using TOPSIS. The main conclusions of this work are as follows:

(1) When the inlet and outlet branch passage inclination ratios are the same, the variation of passage inclination ratio has slight impacts on the cooling capability and the mass flow distribution among the heat transfer microchannels. The mass flow rate of the channels close to the heat sink inlet is smaller than that close to the heat sink outlet, and the non-uniformity of the mass flow distribution along the branch passage results in the uneven temperature distribution. The main causes for this flow maldistribution are upward splashing of inlet fluid and uneven distribution of pressure among the heat transfer microchannels. However, by investigating the effect of inlet and outlet branch passage inclination ratios separately, it is found that the variations of inlet and outlet branch passage inclination ratios vary in the heat transfer characteristics. The larger the inlet passage inclination ratio and the smaller the outlet passage inclination ratio, the more uniform the channel mass flow distribution and the better the cooling capability

(2) When the channel height and channel width ratio are constant, the increase of channel unit width leads to the reduction of heat transfer area and deterioration of cooling performance. Unlike the variation of heat transfer performance, when the channel height or channel width ratio is different, then changing the channel unit width has a different impact on the flow resistance characteristics. The main reason for this phenomenon is that the different combinations of structure parameters result in different flow field structures in the channels. Under the joint influence of sidewall area change and vortex structure change, the pressure drop exhibits different variation patterns with increasing channel unit width.

(3) When investigating the effect of channel unit width and channel width ratio variations, the average temperature of the heat
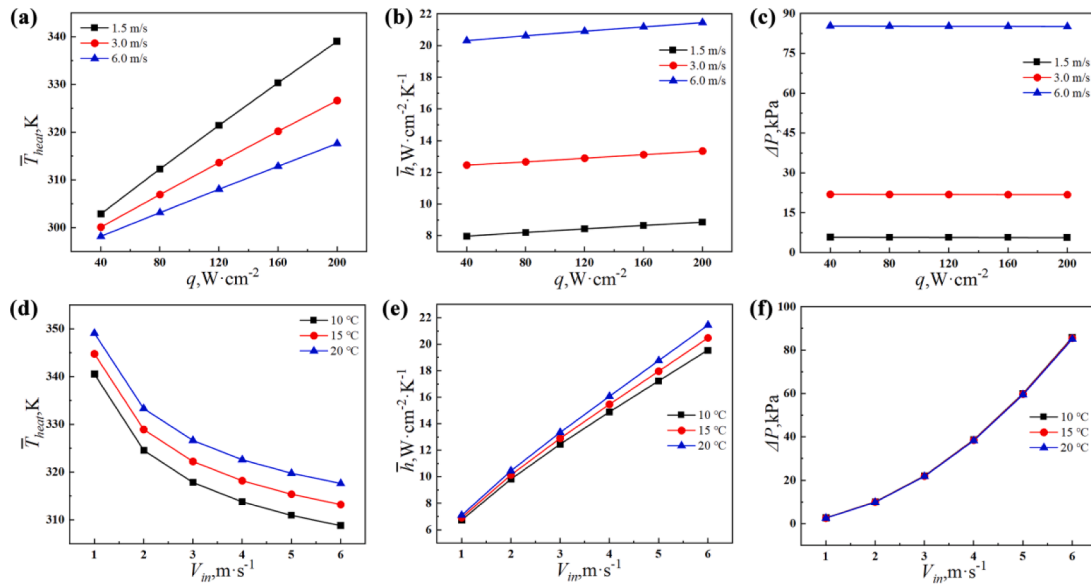


**Fig. 19.** Performances of the different solutions.

**Fig. 20.** Thermal-hydraulic performance under different working conditions.

transfer surface ($\overline{T}_{trans}$) and the average temperature of the heated surface ($\overline{T}_{heat}$) have the same variation trend. However, when investigating the effect of channel height variations, the variation trend of $\overline{T}_{heat}$ is different from the that of $\overline{T}_{trans}$. The primary cause is that the change of channel height will significantly affect the distance from the heat transfer surface to the heated surface, which will impact the thermal resistance. Based on Fourier's law of heat conduction, the thermal resistance variation will change the temperature differential between the heat transfer surface and heated surface. Consequently, the temperature variation trend of the heat transfer surface will not reflect that of the heated surface when the channel height is different.

(4) Both the MOPSO and MOGA can provide reliable Pareto non-inferior solution sets, but the Pareto front obtained by MOGA has a wider range of objective functions in present study. After the optimization, the optimal $\overline{T}_{heat}$ is varied from 316.7 K to 322 K and the optimal $\Delta P$ is varied from 96.1 kPa to 78.6 kPa. Additionally, three solutions on the Pareto front, i.e. the optimal solution C, endpoints A and B, have been modeled and calculated by CFD. Under the same working condition, i.e. $u_{in} = 6$m/s and $q = 200$W/cm$^2$, the numerical values of CFD are basically the same as the predicted values of ANNs and the relative error is small, which further confirms the validity of the ANNs.

(5) By using the classic decision-making algorithm, i.e. TOPSIS, and assigning the equal weighting factor to the two optimization objectives, the geometrical parameters ($W_1 = 1.03$ mm, $\varphi = 0.58$ and $H_3 = 2.44$ mm) are adopted as the optimal compromise solution. Compared with $\overline{T}_{heat}$ minimization, $\Delta P$ of the optimal compromise solution can be reduced by 9 kPa with an increase of 1.4 K in $\overline{T}_{heat}$. Compared with $\Delta P$ minimization, even though $\Delta P$ increase by 8.4 kPa, $\overline{T}_{heat}$ can be reduced by 3.9 K. Additionally, for the optimal compromise solution, with an inlet velocity of 1.5 m/s and a heat flux of 200 W/cm$^2$, the maximum and average temperature of the heated surface does not exceed 73 °C and 67 °C, respectively, and the $\Delta P$ is only 5.7 kPa.

*CRediT authorship contribution statement*

**H.C. Cui:** Conceptualization, Methodology, Software, Validation, Formal analysis, Investigation, Data curation, Writing – original draft,

Writing – review & editing. **C.Y. Shi:** Methodology, Software, Data curation. **M.J. Yu:** Software, Data curation. **Z.K. Zhang:** Software, Data curation. **Z.C. Liu:** Supervision, Project administration, Funding acquisition. **W. Liu:** Resources, Supervision, Project administration, Funding acquisition.

**Declaration of Competing Interest**

The authors declare that they have no known competing financial interests or personal relationships that could have appeared to influence the work reported in this paper.

**Data availability**

Data will be made available on request.

**References**

[1] C. Nadjahi, H. Louahlia, S. Lemasson, A review of thermal management and innovative cooling strategies for data center, Sustain. Computing-Inform. Syst. 19 (2018) 14–28.

[2] S.M.S. Murshed, C.A.N. de Castro, A critical review of traditional and emerging techniques and fluids for electronics cooling, Renew. Sustain. Energy Rev. 78 (2017) 821–833.

[3] J. Lee, I. Mudawar, Low-Temperature Two-Phase Microchannel Cooling for High-Heat-Flux Thermal Management of Defense Electronics, IEEE Trans. Compon. Packag. Technol. 32 (2009) 453–465.

[4] I. Mudawar, Recent Advances in High-Flux, Two-Phase Thermal Management, Journal of Thermal Science and Engineering Applications 5 (2013), 021012.

[5] A.S. Bahman, F. Blaabjerg, Ieee, Optimization Tool for Direct Water Cooling System of High Power IGBT Modules, in: 18th European Conference on Power Electronics and Applications (EPE), Germany, 2016.

[6] F.J. Hong, C.Y. Zhang, W. He, P. Cheng, G. Chen, Confined jet array impingement boiling of subcooled aqueous ethylene glycol solution, Int. Commun. Heat Mass Transfer 56 (2014) 165–173.

[7] D.B. Tuckerman, R.F.W. Pease, High-performance heat sinking for VLSI, IEEE Electron Device Lett. 2 (1981) 126–129.

[8] Q.F. Zhu, H.X. Xia, J.J. Chen, X.M. Zhang, K.P. Chang, H.W. Zhang, H. Wang, J. F. Wan, Y.Y. Jin, Fluid flow and heat transfer characteristics of microchannel heat sinks with different groove shapes, Int. J. Therm. Sci. 161 (2021), 106721.

[9] M. Magnini, O.K. Matar, Numerical study of the impact of the channel shape on microchannel boiling heat transfer, Int. J. Heat Mass Transf. 150 (2020), 119322.

[10] G.D. Xia, D.D. Ma, Y.L. Zhai, Y.F. Li, R. Liu, M. Du, Experimental and numerical study of fluid flow and heat transfer characteristics in microchannel heat sink with complex structure, Energ. Conver. Manage. 105 (2015) 848–857.

[11] H.A. Mohammed, P. Gunnasegaran, N.H. Shuaib, Influence of channel shape on the thermal and hydraulic performance of microchannel heat sink, Int. Commun. Heat Mass Transfer 38 (2011) 474–480.

[12] Y. Hadad, B. Ramakrishnan, R. Pejman, S. Rangarajan, P.R. Chiarot, A. Pattamatta, B. Sammakia, Three-objective shape optimization and parametric study of a micro-channel heat sink with discrete non-uniform heat flux boundary conditions, Appl. Therm. Eng. 150 (2019) 720–737.

[13] Y.L. Zhai, Z.H. Li, H. Wang, J.X. Xu, Thermodynamic analysis of the effect of channel geometry on heat transfer in double-layered microchannel heat sinks, Energ. Conver. Manage. 143 (2017) 431–439.

[14] A. Rajalingam, S. Chakraborty, Effect of shape and arrangement of micro-structures in a microchannel heat sink on the thermo-hydraulic performance, Appl. Therm. Eng. 190 (2021) 116755.

[15] R. A, S. Chakraborty, Effect of micro-structures in a microchannel heat sink – A comprehensive study, Int. J. Heat Mass Transfer, 154 (2020) 119617.

[16] A.F. Al-Neama, Z. Khatir, N. Kapur, J. Summers, H.M. Thompson, An experimental and numerical investigation of chevron fin structures in serpentine minichannel heat sinks, Int. J. Heat Mass Transf. 120 (2018) 1213–1228.

[17] G.L. Wang, D. Niu, F.Q. Xie, Y. Wang, X.L. Zhao, G.F. Ding, Experimental and numerical investigation of a microchannel heat sink (MCHS) with micro-scale ribs and grooves for chip cooling, Appl. Therm. Eng. 85 (2015) 61–70.

[18] M.K. Sung, I. Mudawar, Effects of jet pattern on single-phase cooling performance of hybrid micro-channel/micro-circular-jet-impingement thermal management scheme, Int. J. Heat Mass Transf. 51 (2008) 4614–4627.

[19] Z.Q. He, Y.F. Yan, Z.E. Zhang, Thermal management and temperature uniformity enhancement of electronic devices by micro heat sinks: A review, Energy 216 (2021) 119223.

[20] A.M. Kiper, Impinging water jet cooling of VLSI circuits, Int. Commun. Heat Mass Transfer 11 (1984) 517–526.

[21] P. McInturff, M. Suzuki, P. Ligrani, C. Nakamata, D.H. Lee, Effects of hole shape on impingement jet array heat transfer with small-scale, target surface triangle roughness, Int. J. Heat Mass Transf. 127 (2018) 585–597.

[22] E.N. Wang, L. Zhang, L.N. Jiang, J.M. Koo, J.G. Maveety, E.A. Sanchez, K. E. Goodson, T.W. Kenny, Micromachined jets for liquid impingement cooling of VLSI chips, J. Microelectromech. Syst. 13 (2004) 1072.

[23] X. Du, Z. Yang, H. Zhou, Q. Li, Z. Jin, Numerical investigation of geometry effects on flow, heat transfer and defrosting characteristics of a simplified automobile windshield with a single row of impinging jets, in: SAE Technical Paper, 2016, pp. 0148-7191.

[24] A.J. Robinson, E. Schnitzler, An experimental investigation of free and submerged miniature liquid jet array impingement heat transfer, Exp. Therm. Fluid Sci. 32 (2007) 1–13.

[25] P. Sullivan, S. Ramadhyani, F. Incropera, Use of smooth and roughened spreader plates to enhance impingement cooling of small heat sources with single circular liquid jets, Topics Heat Transf. HTD 206-2 (1993) 103–110.

[26] H.C. Cui, J.H. Xie, R.Z. Zhao, M.Z. Wang, Z.C. Liu, W. Liu, Thermal-hydraulic performance analysis of a hybrid micro pin-fin, jet impingement heat sink with non-uniform heat flow, Appl. Therm. Eng. 208 (2022) 118201.

[27] M.K. Sung, I. Mudawar, Experimental and numerical investigation of single-phase heat transfer using a hybrid jet-impingement/micro-channel cooling scheme, Int. J. Heat Mass Transf. 49 (2006) 682–694.

[28] Y.J. Zhang, S.F. Wang, P.X. Ding, Effects of channel shape on the cooling performance of hybrid micro-channel and slot-jet module, Int. J. Heat Mass Transf. 113 (2017) 295–309.

[29] Z. Deng, J. Shen, W. Dai, Y.W. Liu, Q.L. Song, W.C. Gong, L. Ke, M.Q. Gong, Flow and thermal analysis of hybrid mini-channel and slot jet array heat sink, Appl. Therm. Eng. 171 (2020) 115063.

[30] F. Zhou, Y. Liu, Y.H. Liu, S.N. Joshi, E.M. Dede, Modular Design for a Single-Phase Manifold Mini/Microchannel Cold Plate, J. Therm. Sci. Eng. Appl. 8 (2016), 021010.

[31] F. Zhou, E.M. Dede, S.N. Joshi, Ieee, A Novel Design of Hybrid Slot Jet and Mini-Channel Cold Plate for Electronics Cooling, in: 31st Annual Semiconductor Thermal Measurement, Modeling and Management Symposium (SEMI-THERM), San Jose, CA, 2015, pp. 60-67.

[32] A.J. Robinson, R. Kempers, J. Colenbrander, N. Bushnell, R. Chen, A single phase hybrid micro heat sink using impinging micro-jet arrays and microchannels, Appl. Therm. Eng. 136 (2018) 408–418.

[33] W. Gao, J.F. Zhang, Z.G. Qu, W.Q. Tao, Numerical investigations of heat transfer in hybrid microchannel heat sink with multi-jet impinging and trapezoidal fins, Int. J. Therm. Sci. 164 (2021) 106902.

[34] X.M. Huang, W. Yang, T.Z. Ming, W.Q. Shen, X.F. Yu, Heat transfer enhancement on a microchannel heat sink with impinging jets and dimples, Int. J. Heat Mass Transf. 112 (2017) 113–124.

[35] A. Husain, M. Ariz, N.Z.H. Al-Rawahi, M.Z. Ansari, Thermal performance analysis of a hybrid micro-channel, -pillar and -jet impingement heat sink, Appl. Therm. Eng. 102 (2016) 989–1000.

[36] S. Ndao, H.J. Lee, Y. Peles, M.K. Jensen, Heat transfer enhancement from micro pin fins subjected to an impinging jet, Int. J. Heat Mass Transf. 55 (2012) 413–421.

[37] S. Ndao, Y. Peles, M.K. Jensen, Multi-objective thermal design optimization and comparative analysis of electronics cooling technologies, Int. J. Heat Mass Transf. 52 (2009) 4317–4326.

[38] F.L. Cui, F.J. Hong, P. Cheng, Comparison of normal and distributed jet array impingement boiling of HFE-7000 on smooth and pin-fin surfaces, Int. J. Heat Mass Transf. 126 (2018) 1287–1298.

[39] C.U. Gonzalez-Valle, S. Samir, B. Ramos-Alvarado, Experimental investigation of the cooling performance of 3-D printed hybrid water-cooled heat sinks, Appl. Therm. Eng. 168 (2020), 114823.

[40] E. Masanet, A. Shehabi, N. Lei, S. Smith, J. Koomey, Recalibrating global data center energy-use estimates, Science 367 (2020) 984–986.

[41] H. Tan, P.A. Du, K. Zong, G.Y. Meng, X. Gao, Y. Li, Investigation on the temperature distribution in the two-phase spider netted microchannel network heat sink with non-uniform heat flux, Int. J. Therm. Sci. 169 (2021), 107079.

[42] H.C. Cui, X.T. Lai, J.F. Wu, M.Z. Wang, W. Liu, Z.C. Liu, Overall numerical simulation and experimental study of a hybrid oblique-rib and submerged jet impingement/microchannel heat sink, Int. J. Heat Mass Transf. 167 (2021), 120839.

[43] P.J. Roache, Perspective: A Method for Uniform Reporting of Grid Refinement Studies, J. Fluids Eng. 116 (1994) 405–413.

[44] X. Du, Z. Yang, Z. Jin, C. Xia, D. Bao, A comparative study of passive control on flow structure evolution and convective heat transfer enhancement for impinging jet, Int. J. Heat Mass Transf. 126 (2018) 256–280.

[45] Z. Hernádi, G. Kristóf, Prediction of pressure drop and heat transfer coefficient in helically grooved heat exchanger tubes using large eddy simulation, Proceedings of the Institution of Mechanical Engineers, Part A: Journal of Power Energy, 228 (2014) 317-327.

[46] M.K. Sung, I. Mudawar, Single-phase and two-phase heat transfer characteristics of low temperature hybrid micro-channel/micro-jet impingement cooling module, Int. J. Heat Mass Transf. 51 (2008) 3882–3895.

[47] Y. Zhang, S. Wang, Z. Liu, Effect of fluid distribution on the cooling performance of hybrid microchannel and slot-jet impingement system, Appl. Therm. Eng. 222 (2023), 119913.

[48] Z. Tan, P. Jin, Y. Zhang, G. Xie, Flow and thermal performance of a multi-jet twisted square microchannel heat sink using CuO-water nanofluid, Appl. Therm. Eng. 225 (2023), 120133.

[49] A.K. Jaiswal, P.S. Mahapatra, B.V.S.S.S. Prasad, Effect of microchannel on combined impingement and film cooling of a concave surface, Int. Commun. Heat Mass Transfer 126 (2021) 105441.

[50] K. Deb, A. Pratap, S. Agarwal, T. Meyarivan, A fast and elitist multiobjective genetic algorithm: NSGA-II, IEEE Trans. Evol. Comput. 6 (2002) 182–197.

[51] C.A.C. Coello, G.T. Pulido, M.S. Lechuga, Handling multiple objectives with particle swarm optimization, IEEE Trans. Evol. Comput. 8 (2004) 256–279.

[52] Y.H. Lin, Y. Luo, W. Li, Y.L. Cao, Z. Tao, T.I.P. Shih, Single-phase and Two-phase Flow and Heat Transfer in Microchannel Heat Sink with Various Manifold Arrangements, Int. J. Heat Mass Transf. 171 (2021), 121118.

[53] C.S. Sharma, M.K. Tiwari, S. Zimmermann, T. Brunschwiler, G. Schlottig, B. Michel, D. Poulikakos, Energy efficient hotspot-targeted embedded liquid cooling of electronics, Appl. Energy 138 (2015) 414–422.

[54] C.S. Sharma, G. Schlottig, T. Brunschwiler, M.K. Tiwari, B. Michel, D. Poulikakos, A novel method of energy efficient hotspot-targeted embedded liquid cooling for electronics: An experimental study, Int. J. Heat Mass Transf. 88 (2015) 684–694.

[55] C.-L. Hwang, Y.-J. Lai, T.-Y. Liu, A new approach for multiple objective decision making, Comput. Oper. Res. 20 (1993) 889–899.